Lock Acquisition in Resonant Optical Interferometers

Thesis by

Matthew Evans

In Partial Fulfillment of the Requirements

for the Degree of

Doctor of Philosophy

California Institute of Technology

Pasadena, California

2002

(Submitted December 12, 2001)

Abstract

The LIGO (Laser Interferometric Gravitational-wave Observatory) project, and other projects around the world, are currently planning to use long-baseline (> 1 km) interferometers to directly detect gravitational radiation from astrophysical sources. In this work we present a framework for lock acquisition, the process by which an initially uncontrolled resonant interferometer is brought to its operating point. Our approach begins with the identification of a path which takes the detector from the uncontrolled state to the operational state. The properties of the detector's outputs along this path, embodied in the sensing matrix, must be determined and parameterized in terms of measureables. Finally, a control system which can compute the inverse of the sensing matrix, apply it to the incoming signals, and make the resulting signals available for feedback is needed to close the control loop. This formalism was developed and explored extensively in simulation and was subsequently applied to the LIGO interferometers. Results were in agreement with expectation within error, typically $\pm 20\%$ on the sensing matrix elements, and the method proved capable of bringing a high-finesse power-recycled Fabry-Perot-Michelson interferometer (a LIGO detector) to its operating point.

Acknowledgements

In the journey that has taken me from a naive and vague thesis topic to a solid and experimentally verified contribution to the scientific community, I have met and worked with many fine people. Among those that I have leaned on the most are Peter Fritschel, Nergis Mavalvala and Stan Whitcomb. These people have showed me kindness and patience beyond any that I could have expected or asked for.

I would like to single out Nergis for the many hours she endured in my company and the friendship she bestowed upon me despite it all. To quote James Mason "Nergis Mavalvala has always been a font of wisdom and pillar of support. Do *not* believe her modesty, sincere as it may be. She's brilliant." I couldn't agree more.

The contributions made to my work by the modeling group are manifold, as are my thanks to them. It was through the simulation tools on which they worked that was able to develop and test various lock acquisition strategies, thereby gaining an understanding of the problem not available by any other means. Hiro Yamamoto in particular graced me with many hours of discussion through which I have not only become a better programmer, but also a better physicist.

More broadly, I would like to thank all the people on the LIGO team. In some cases I had the pleasure of interacting directly with the people that made my work possible, but I'm sure there are many that I relied on without ever recognizing their contribution or thanking them for it. I would like to take this opportunity to express my gratitude to all of these people for their support.

There are a number of professors from who's time and council I have benefited over the years. Barry Barish, Ken Libbrecht, Tom Prince, Kip Thorne, Robbie Vogt, and Alan Weinstein have all helped to guide me along the path to my graduation, ushering me past the milestones, and pulling me from the bogs.

My office mates, Adam Chandler, Rick Jenet, James Mason, Malik Rakhman, and Chip Sumner, should not be forgotten here. They have been my study partners, my

counselors, my chauffeurs, and my drinking buddies. It was they who kept me sane through the countless hours in the office and offered me the kind of sage advice you can only get from those who are in the boat with you.

I will not try to enumerate the contributions of my loved ones for their roles in my life are beyond words. I am grateful to all of you for bringing me to this point and continuing on with me as I move into the unknown.

Contents

Abstract iii

Acknowledgements iv

1 Introduction 1

1.1 Gravitational Waves: A New Window 1

1.2 Interferometer Configurations 3

1.2.1 Michelson 3

1.2.2 Fabry-Perot Arm Cavities 4

1.2.3 Power Recycling 6

1.2.4 Dual Recycling 7

1.3 Purpose of this Work 7

2 Basic Formalism 10

2.1 Surfaces and Spaces 10

2.2 Modulation and Demodulation 12

2.3 The End-To-End Model 14

3 A Simple System: The Fabry-Perot Cavity 16

3.1 Optical Configuration 16

3.2 Near Resonance Control 17

3.3 Lock Acquisition Threshold Velocity 20

3.4 Simple Lock Acquisition 21

3.5 Guided Lock Acquisition 21

3.6 Error Signal Linearization 23

4 Complex Resonant Systems **27**

4.1 The Sensing Matrix 27

4.1.1 Fabry-Perot Cavity Sensing Matrix 29

4.1.2 LIGO 1 Sensing Matrix 30

4.2 The Input Matrix 33

4.2.1 No Signal Singularities 34

4.2.2 Degenerate Signal Singularities 35

4.3 Multi-Step Lock Acquisition 35

4.3.1 State 1 35

4.3.2 State 2 36

4.3.3 State 3 36

4.3.4 State 4 37

4.3.5 State 5 37

4.4 Frequency Response 38

5 Experiment **41**

5.1 Experimental Setup 41

5.1.1 The Analog and Optical Hardware 41

5.1.2 The Digital Control System 43

5.1.3 Sources of Excitation 45

5.2 Detection Mode Control Scheme 46

5.3 Sensing Matrix Estimation 47

5.3.1 Field Amplitude Estimators 47

5.3.2 Calibration of Power Signals 52

5.3.3 Gain Coefficients 53

5.4 Implementation 54

5.4.1 Discontinuous Changes: Triggers and Bits 55

5.4.2 Continuous Changes: The Input Matrix in Each State 56

5.5 Experimental Results 58

6 Conclusion **60**

A The Fabry-Perot Cavity **62**

A.1 Cavity Statics 62

A.2 Cavity Dynamics 63

B Notational Conventions **69**

B.1 Notational Conventions 69

B.2 Symbol Glossary 70

B.2.1 General 70

B.2.2 Chapter 1 70

B.2.3 Chapter 2 71

B.2.4 Chapter 3 71

B.2.5 Chapter 4 72

B.3 Normalized Determinant 72

Bibliography **74**

List of Figures

1.1 Strain from a gravitational wave 2
1.2 A Michelson interferometer. 4
1.3 A Fabry-Perot-Michelson interferometer. 5
1.4 A power recycled interferometer. 6
1.5 A dual recycled interferometer. 8

2.1 Notational conventions for a surface. 10
2.2 The distance between two surfaces. 12

3.1 Optical layout of a Fabry-Perot cavity. 16
3.2 The Pound-Drever-Hall error signal for a Fabry-Perot cavity. 18
3.3 Threshold velocity in a simple lock acquisition model. 20
3.4 Threshold velocity in a more realistic lock acquisition model. 22
3.5 Error signal linearization. 24
3.6 Threshold velocity with error signal linearization, simulated. 25
3.7 Threshold velocity with error signal linearization, experimental. . . . 26

4.1 LIGO 1 optical layout. 30
4.2 Simulated lock acquisition event 38

5.1 Experimental apparatus conceptual pieces. 41
5.2 LIGO Hanford 2 km optical layout. 42
5.3 Seismic noise 45
5.4 Frequency noise 46
5.5 Hanford 2k lock acquisition event 59

A.1 Deformed contour integral segments. $\xi \equiv [i-1]\,\eta_I$ 64
A.2 Alternate contour. $\bar{\xi} \equiv \frac{[\eta_R - \eta_I]}{\sqrt{2i}}$ 67

A.3 Cavity response to a fixed velocity sweep. 68

List of Tables

5.1 LIGO 1 optical parameters. 43
5.2 LIGO 1 digital filter bank. 44

Chapter 1

Introduction

1.1 Gravitational Waves: A New Window

For all of recorded history astronomers have peered skyward and observed the wonders of the universe through an ever broadening range of electromagnetic radiation. Einstein's theory of general relativity predicts another form of radiation; ripples in the very fabric of space-time produced by accelerating aspherical mass distributions. These propagating deformations of space-time are known as "gravitational waves" and they offer a new window through which to view the physical universe. This window promises a view of exotic and as yet poorly understood objects, but more importantly it promises a view of the unknown. In physics, as in life, it is through encounters with the unknown that we are most dramatically challenged to expand our understanding.

Sources of gravitational waves strong enough to be detected by a ground-based detector are limited to phenomena that explore the most extreme conditions conceivable in the context of general relativity with the source density approaching the point of gravitational collapse into a black hole and the source motion approaching the speed of light.[1] Sources are further limited by the asymmetric nature of the motion required, since the lowest order mass distribution which can produce gravitational radiation is the quadrupole moment, the monopole moment being fixed by mass-energy conservation and oscillation of the dipole moment forbidden by momentum conservation. Despite these limitations, there are several candidates among the known astrophysical phenomena which might produce detectable gravitational waves, including supernova explosions, coalescing compact binaries, and spinning neutron stars, just to list a few.

Gravitational radiation, due to its quadrupolar nature, produces a oscillating shear strain in space transverse to the propagation direction. The effect that the passage

of such a wave would have on a ring of inertial masses is shown in figure 1.1. The quantity used to express the amount of spatial deformation resulting from a passing gravitational wave, also shown in figure 1.1, is called "strain" and is typically identified with the letter h. Strain may be expressed as a fractional change in some spatial dimension, L, as

$$h = 2\frac{\Delta L}{L}. \tag{1.1}$$

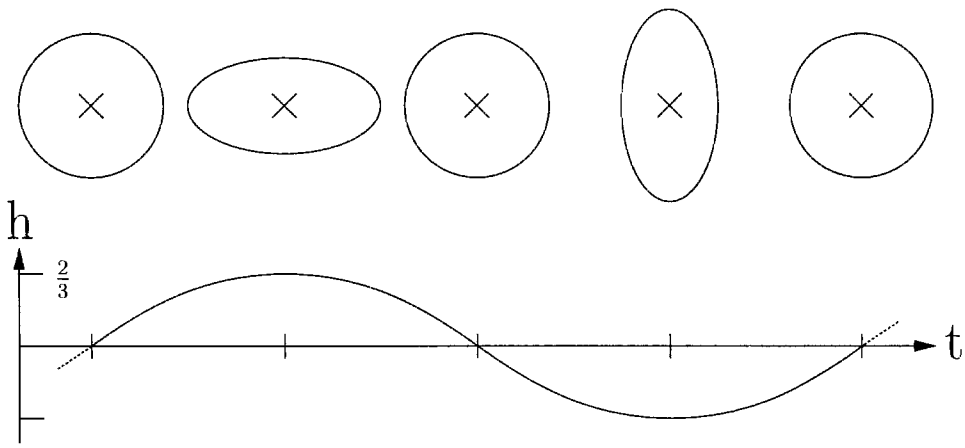

Figure 1.1: Strain from a gravitational wave traveling into the page would deform a ring of inertial test masses as shown. The amount of strain depicted, however, is about 21 orders of magnitude greater than an earth-based observer should expect from anticipated astrophysical sources.

The coalescing neutron star binary, due to its relative simplicity, limited range of parameters, and status as the only system experimentally (though indirectly) observed to emit gravitational radiation, sets the scale for ground-based gravitational wave detector sensitivity. A coalescence of this sort in the Virgo cluster, which as the nearest major galaxy cluster is the most likely nearby source of events, would typically produce strains of order $h \sim 10^{-21}$.[2] The volume of space covered by a detector capable of detecting such an event contains of several thousand galaxies and is likely to produce a neutron star binary coalescence every few years.[3]

1.2 Interferometer Configurations

The idea of using interferometry as a means of gravitational wave detection was first proposed in the 1960s ([4] referenced by Thorne in [5]) and 1970s.[6, 7] The following sections explore the evolution of optical configurations proposed for use in gravitational wave detection.[8, 9]

1.2.1 Michelson

The Michelson interferometer has been used for more than a century as a sensitive measurement device and is the cornerstone for all of the gravitational wave detectors discussed in the following sections. The signal produced by this type of detector is proportional to the differential phase shift of the light returning to the beam-splitter (BS, see figure 1.2) produced by differential changes in the lengths of the two arms. The expression for the phase difference produced by a low frequency gravitational wave with optimal orientation and polarization is

$$\phi = 2kLh \tag{1.2}$$

where L is the unperturbed arm length and k is the wave-number of the light[1] used in the interferometer. Through "frontal" or "Schnupp" modulation, and other methods, a detector placed at the "anti-symmetric port" (ASY) can be made to measure ϕ, and thus detect the wave's passage.[10] Equation (1.2) can be rewritten to characterize the sensitivity of a detector as

$$\Delta h = \frac{\Delta\phi}{2kL} \tag{1.3}$$

where $\Delta\phi$ represents the noise in the phase measurement and Δh is the corresponding minimum measurable strain.

For ground-based detectors, practical considerations limit L to a few kilometers and k to values of order $10^7/\,\mathrm{m}$; thus for a Michelson interferometer to serve as an

[1] The word "light" will be used liberally in this work and should most often be read as "electromagnetic radiation."

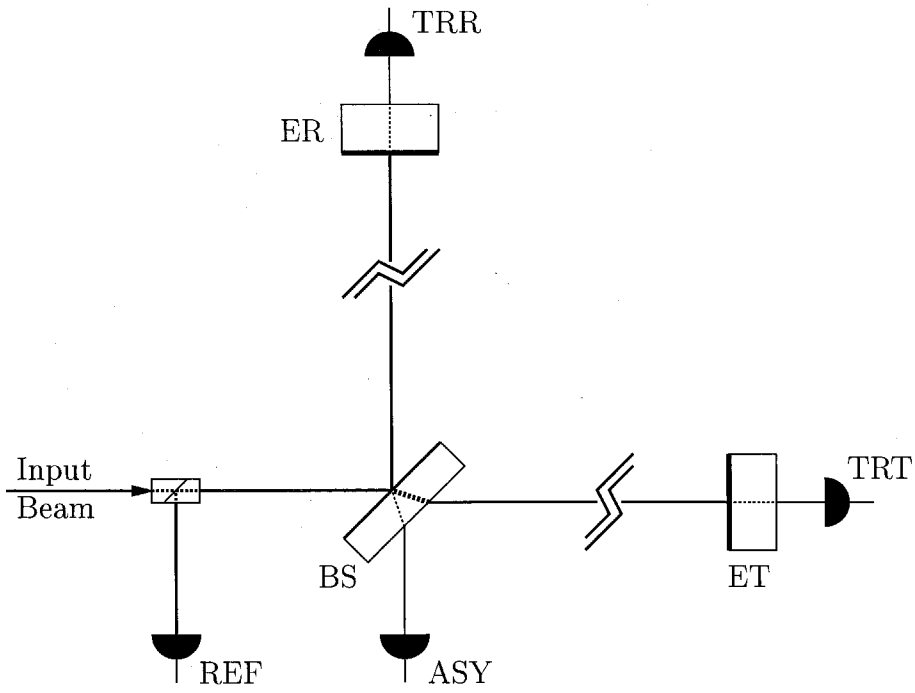

Figure 1.2: A Michelson interferometer.

effective gravitational wave detector it should be sensitive to $\Delta\phi \sim 10^{-11}$. Various noise sources, which are discussed elsewhere in considerable depth, make this level of phase sensitivity extremely difficult to attain.[11, 12]

1.2.2 Fabry-Perot Arm Cavities

The simplicity of equation (1.3) does not allow for a great variety of approaches to increasing the sensitivity, given by $1/\Delta h$, of a Michelson based interferometer. There are only two clear avenues of attack on the impracticality of a simple Michelson interferometer: increasing the effective length L or decrease the phase noise $\Delta\phi$. The "Fabry-Perot-Michelson" detector configuration, representative of the only currently operational interferometric gravitational wave detector, takes the first of these two routes.[13]

A more descriptive name for this configuration might be a "Michelson-interferometer with Fabry-Perot arm cavities." The Fabry-Perot arm cavities result from the addition of two "Input Test Masses" (IT and IR). Light which enters an arm cavity

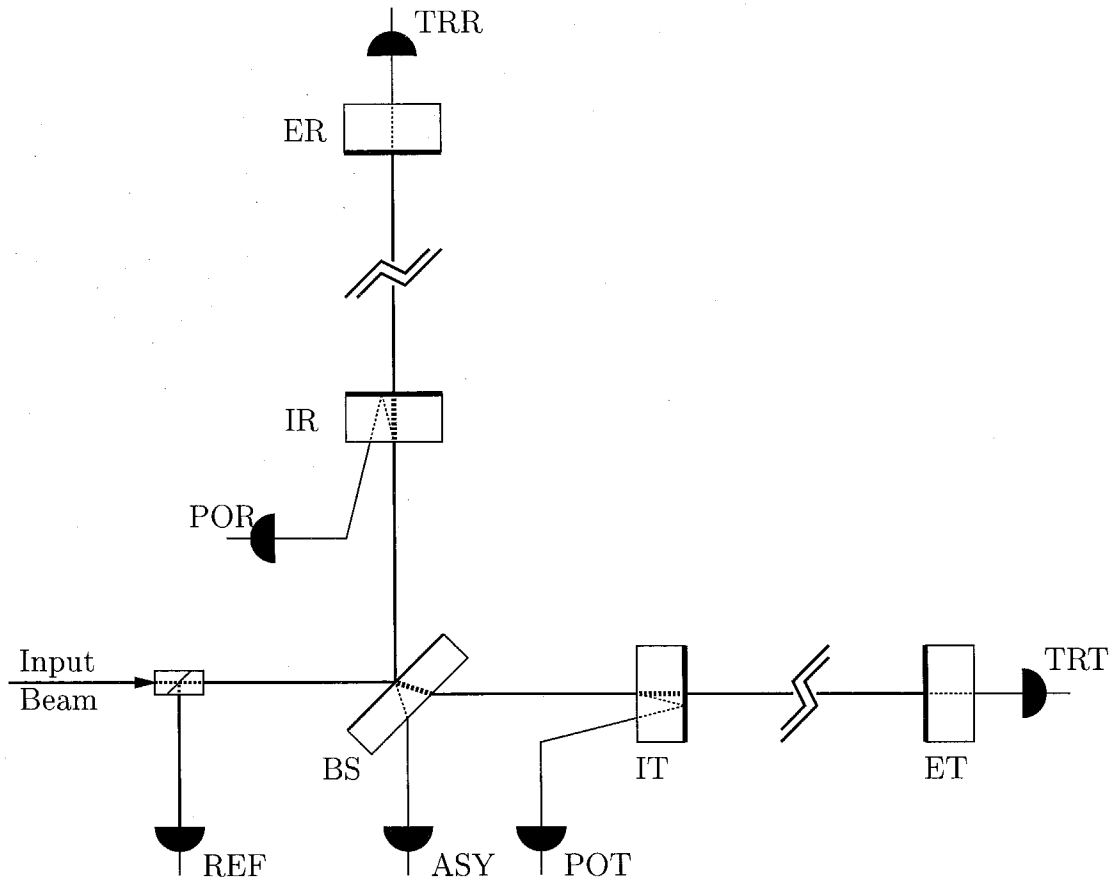

Figure 1.3: A Fabry-Perot-Michelson interferometer.

samples the space between the input and end test masses of that cavity multiple times before returning to the beam-splitter. For this reason the cavities act as leaky integrators of phase shift in the arms and serve to increase the sensitivity of the interferometer at low frequencies, typically by two or three orders of magnitude.[14]

There is, however, a caveat to the use of Fabry-Perot cavities to increase sensitivity: a cavity only integrates effectively if the light circulating in the cavity interferes constructively with the light entering the cavity. This amounts to the requirement that the round-trip phase in the cavity be close[2] to an integer multiple of 2π, which in turn defines an operating point that must be arrived at and maintained for the interferometer to function properly.

[2]The meaning of "close" is determined by the properties of the cavity and will be discussed in detail in section 3.2.

"Lock acquisition" is the process by which an uncontrolled interferometer is brought to and held at its operating point. This is not particularly challenging for Fabry-Perot-Michelson interferometers since the two pick-off ports (POT and POR) can be used to measure the light returning from each cavity independent of the other, thereby reducing lock acquisition in this configuration to the largely solved problem of locking a single cavity.[15] Lock acquisition in a single Fabry-Perot cavity, however, serves as the foundation for a more general discussion and is the subject of chapter 3.

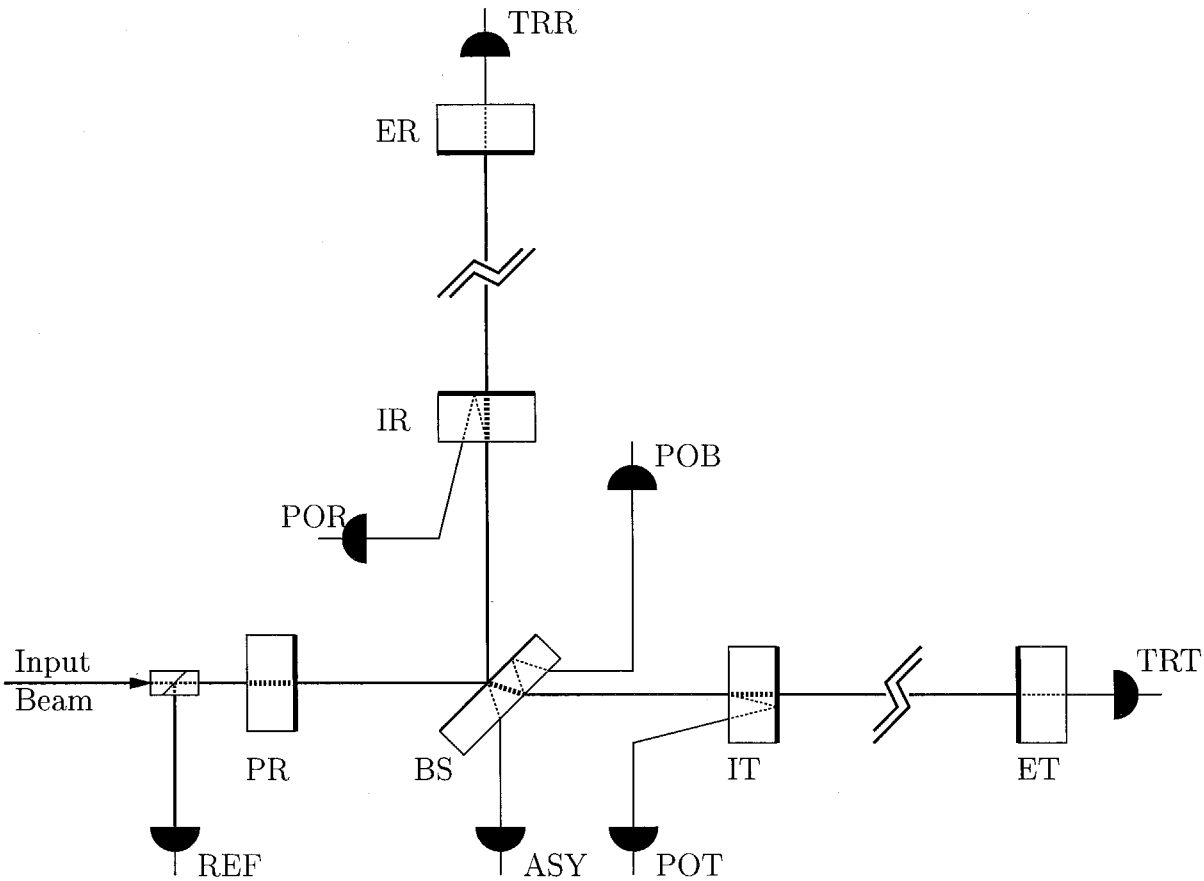

Figure 1.4: A power recycled interferometer.

1.2.3 Power Recycling

Many of the detectors that will begin to collect data in the coming years are "Power Recycled" interferometers.[8] This configuration adds an optic, the "Power Recycling

Mirror" (PR), to the Fabry-Perot-Michelson configuration. While this addition does not significantly change the response of the interferometer to gravitational waves, it allows the interferometer to operate at higher power than would otherwise be possible. More photons in the interferometer implies better detection statistics, which in turn decreases $\Delta\phi$ by as much as the square-root of the power increase.[16, 17]

Unfortunately, the addition of the recycling mirror brings with it another cavity which must also be resonant. Even more troubling is the fact that power recycling mixes the control signals from the two arms and fundamentally changes the dynamics of the interferometer to that of a coupled cavity system. These changes complicate the control of the interferometer and add considerable spice to the associated lock acquisition problem.

The experimental work presented in chapter 5 was performed with a power recycled interferometer. This configuration also serves as the canonical example in the more general discussion of lock acquisition presented in chapter 4.

1.2.4 Dual Recycling

The next generation of detectors will consist largely of "Dual Recycled" interferometers. The dual recycled configuration includes a "Signal Recycling Mirror" (SR) at the anti-symmetric port and allows the interferometer to be tuned for increased sensitivity to gravitational waves in some frequency range. It also complicates the already difficult acquisition and control problem.[18] While this work does not specifically address the dual recycled configuration, it is intended to be sufficiently general to guide the designers of this and other configurations to a workable lock acquisition scheme.

1.3 Purpose of this Work

There are currently several research efforts worldwide that are developing large scale interferometers for gravitational wave detection. Many of the detectors, including LIGO,[19] VIRGO,[20] and TAMA [13] will adopt a power recycled configuration.

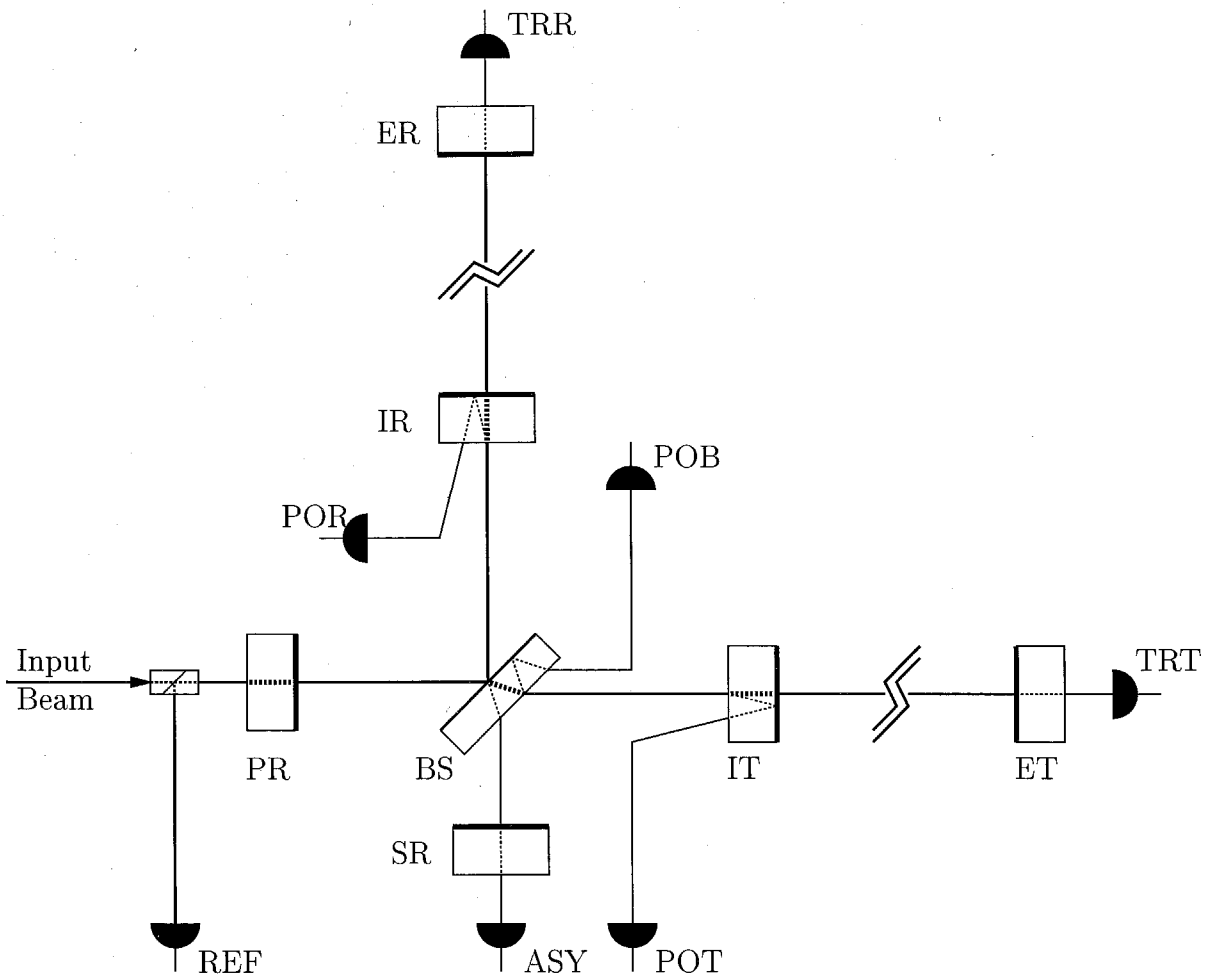

Figure 1.5: A dual recycled interferometer.

Both LIGO and VIRGO are multi-kilometer efforts; LIGO has 4 km arms and VIRGO is 3 km. The TAMA project in Tokyo is an order of magnitude smaller, at 300 m.

Lock acquisition is a necessary step in the operation of all current interferometric gravitational wave detectors and is likely to remain so for many years to come. While the problem of lock acquisition has been addressed anecdotally by the builders of many prototype interferometers, none have addressed the problem in general. Prototypes inherently avoid some of the potential complexities of lock acquisition by reduction of the scale of the interferometer, construction as fixed mass interferometers,[21, 2] reduction of the number resonant cavities,[22, 23] and/or reduction of signal mixing and control requirements through artificially low mirror reflectivities.[13, 18] A case-

by-case post hoc approach has been sufficient for prototype interferometers because of the relaxed, or non-existent, sensitivity requirements placed on them. However, in the absence of a firm understanding of the lock acquisition process, detectors must either be limited to systems which avoid complex lock acquisition problems, or risk being inoperable until they can be retrofitted or redesigned for lock acquisition.

A clear demonstration of the importance of understanding lock acquisition occurred at the 40m LIGO prototype interferometer. This interferometer was designed to be similar to the power-recycled first generation LIGO detectors, but with arms 100 times shorter. Despite many months of work, the prototype could only be locked intermittently and there was no clear understanding of the lock acquisition process.

As experimental verification of its applicability, this work has been applied to the problem of lock acquisition in the first generation of LIGO detectors. These power-recycled interferometers have 4 degrees of freedom and 5 error signals with which to hold those degrees of freedom within less than 10^{-10} m of their resonance positions. Over the course of the lock acquisition process, which requires about a second (plenty of time for disaster to strike), the fields in the recycling cavity change dramatically and the power in the arm cavities changes by three orders of magnitude. The changing field amplitudes cause the responses of the error signals to vary in content, strength and, in some cases, sign. Through the framework presented in this work these variations may be understood and compensated for, thereby allowing control of the interferometer to be maintained and the operational state of the detector achieved.

As the LIGO detectors and their international counterparts launch into this inevitable precursory step on the path to robust operation, the need for a general lock acquisition strategy is apparent. The purpose of this work is to provide a general framework for understanding the lock acquisition process and its impact on interferometer design.

Chapter 2

Basic Formalism

2.1 Surfaces and Spaces

In this work fields are treated as plane-waves and surfaces are approximated by flat planes of infinite extent. This treatment is equivalent to using the paraxial approximation under the assumption that all of the optics are well aligned and well matched to the input beam such that all of the field energy starts in, and remains in, the lowest order Hermite-Gaussian mode.[24] While this approach is not sufficient for a general investigation of interferometer behavior, it is sufficient for demonstrating the fundamentals of lock acquisition.

The notation used for specifying the position of a surface and the fields at a surface is shown in figure 2.1. The surface of interest for a given optic is marked with a heavy

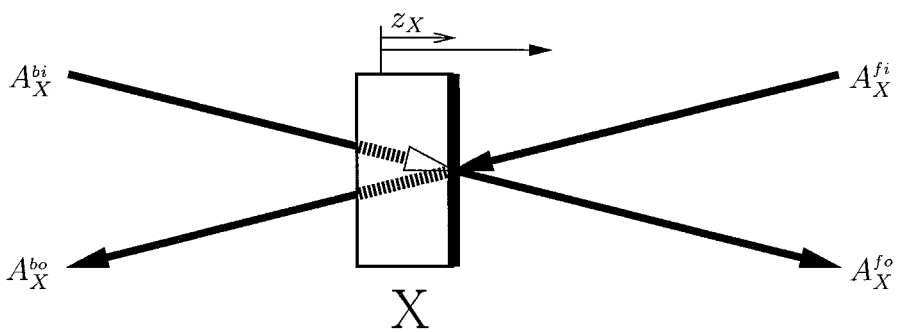

Figure 2.1: Notational conventions for a surface.

line and referred to simply by the name of the optic, in this case X. The position of the surface, z_X, is measured along a coordinate axis normal to the surface and pointing away from the optic's substrate (i.e., into the vacuum). The location of the $z_X = 0$ plane, or "reference plane", on the coordinate axis is arbitrary, but is typically chosen to be near the nominal rest position of the surface if such a position exists.

Note that $z_X > 0$ when the surface is displaced in the positive direction relative to the reference plane, as show in figure 2.1. (In figure 2.2 below, $z_X > 0$ and $z_Y < 0$.)

There are four interacting field amplitudes at each surface. The superscript indicates whether the field is on the front (vacuum side) or back (substrate side) of the surface and whether the field is incoming or outgoing. For instance, A_X^{bi} is the amplitude of the incoming field on the back of surface X. The electric field corresponding to a given field amplitude is

$$E_X = A_X e^{i\omega t} \tag{2.1}$$

where ω, the angular frequency of the field, is related to the wave-number and wavelength of the field by $k = \frac{2\pi}{\lambda} = \frac{\omega}{c}$.

Each reflective surface is characterized by a coefficient of amplitude reflectivity, r_X, and a coefficient of amplitude transmissivity, t_X, which satisfy

$$r_X^2 + t_X^2 \lesssim 1 \tag{2.2}$$

where r_X and t_X are real numbers between 0 and 1. The outgoing fields at the surface are related to the incoming fields by[1]

$$A_X^{fo} = -r_X \, e^{-2ikz_X} \, A_X^{fi} + t_X \, A_X^{bi} \tag{2.3}$$

and

$$A_X^{bo} = r_X \, e^{2ikz_X} \, A_X^{bi} + t_X \, A_X^{fi}. \tag{2.4}$$

As a field propagates from surface X to surface Y it acquires phase according to

$$A_Y^{fi}(t) = e^{ikL_{X:Y}} \, A_X^{fo}\left(t - \frac{L_{X:Y} - z_X - z_Y}{c}\right) \tag{2.5}$$

where $L_{X:Y}$ is the distance between the X and Y reference planes (see figure 2.2). Note that $L_{X:Y}$ does not depend on z_X or z_Y and is, in fact, a time-independent

[1] In the more general case of non-perpendicular incidence, z_X should be replaced by $\cos(\theta_X)\, z_X$, where θ_X is the angle of incidence.

quantity.

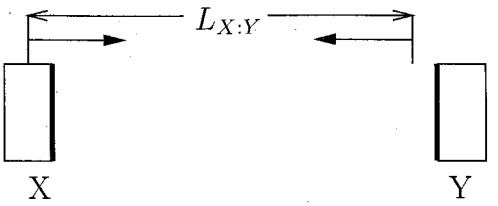

Figure 2.2: The distance between two surfaces.

Though it is not a requirement of this formalism, z_X is typically of order λ and is thought of as representing the microscopic motion of a surface. $L_{X:Y}$, on the other hand, is typically many orders of magnitude greater than λ and is thought of as the macroscopic distance between two surfaces. In this case equation (2.5) can be approximated by

$$A_Y^{fi}(t) \simeq e^{ikL_{X:Y}} \; A_X^{fo}\left(t - \frac{L_{X:Y}}{c}\right) \tag{2.6}$$

which conveniently makes the propagation operation independent of the positions of the surfaces propagated to and from.

In the following chapters, mirror surfaces will generally be given two letter labels and detector surfaces three letter labels. Detector surfaces will be assumed for simplicity to absorb all light incident on them, and thus the direction specification, which is always "fi," will be dropped (e.g., A_{PDX}^{fi} will be written as A_{PDX}.)

2.2 Modulation and Demodulation

All of the interferometer configurations discussed herein rely on phase modulation of the input light and coherent demodulation of the signals from various detectors to produce information about the state of the interferometer. In general, a sinusoidally phase modulated field can be represented by a sum of fields oscillating at different

frequencies as

$$E_{IO}(t) = E_{IN}(t)\, e^{i\Gamma_{mod}\, \sin(\omega_{mod}\, t)} \tag{2.7}$$

$$= E_{IN}(t) \sum_{j=-\infty}^{\infty} J_j(\Gamma_{mod})\, e^{ij\omega_{mod}t} \tag{2.8}$$

where $J_j(x)$ are the Bessel functions, Γ_{mod} is the modulation depth, and ω_{mod} is the modulation frequency. The "Input Beam" in each interferometer configuration is a phase modulated field given by

$$A_{IO_j} = A_{IN}\ J_j(\Gamma_{mod})\,, \text{ and } \omega_{IO_j} = \omega_{IN} + j\ \omega_{mod} \tag{2.9}$$

where A_{IN} and ω_{IN} are the pre-modulation values of the field amplitude and frequency. The frequency components of the Input Beam propagate through the interferometer independently, interacting only at the photo-detectors.

Though far from reality, it is sufficient in this work to consider idealized photo-detectors which produce a signal that is simply proportional to the light power incident on them at any point in time

$$S_{det} = \sum_{j,k} A^{\star}_{DET_j} A_{DET_k} e^{i[\omega_j - \omega_k]t}. \tag{2.10}$$

Coherent demodulation by an equally idealized mixer produces a "demod signal" given by

$$S_{demod} = \frac{1}{t_1 - t_0} \int_{t_0}^{t_1} dt\ S_{det} \sin(\omega_{demod} t + \phi_{demod}) \tag{2.11}$$

where ϕ_{demod} is the demodulation phase, and $\omega_{demod} = n\omega_{mod}$ with $n = 1$ being the most typical form of demodulation. Substituting in the definition of S_{det} and

rearranging terms leads to a more suggestive form

$$\begin{aligned} S_{demod} &= \frac{1}{t_1 - t_0} \int_{t_0}^{t_1} dt \; \mathcal{I}m\left(S_{det} e^{i[\omega_{demod} t + \phi_{demod}]}\right) \\ &= \frac{1}{t_1 - t_0} \int_{t_0}^{t_1} dt \; \mathcal{I}m\left(e^{i\phi_{demod}} \sum_{j,k} A^{\star}_{DET_j} A_{DET_k} e^{i[\omega_{demod} + \omega_j - \omega_k]t} \right) \\ &= \mathcal{I}m\left(e^{i\phi_{demod}} \sum_{j,k} \frac{A^{\star}_{DET_j} A_{DET_k}}{t_1 - t_0} \int_{t_0}^{t_1} dt \; e^{i[\omega_{demod} + \omega_j - \omega_k]t} \right). \end{aligned}$$

Given that $t_1 - t_0 \gg 1/\omega_{mod}$, only the lowest frequency component of S_{demod} survives integration

$$S_{demod} = \mathcal{I}m\left(e^{i\phi_{demod}} \sum_{j,k} A^{\star}_{DET_j} A_{DET_k} \delta_{j+n,k} \right) \tag{2.12}$$

$$= \mathcal{I}m\left(e^{i\phi_{demod}} \sum_{j} A^{\star}_{DET_j} A_{DET_{j+n}} \right). \tag{2.13}$$

Equation (2.13) is the basis for all of the demod signals used in this work. Only small modulation depths ($\Gamma_{mod} < 1$) will be considered herein, which usually means that E_{IO} may be well approximated by truncating the sum in equation (2.8) to contain only $j \in \{-1, 0, 1\}$, such that equation (2.13) reduces to

$$S_{demod} = \mathcal{I}m\left(e^{i\phi_{demod}} \left[A^{\star}_{DET_{-1}} \; A_{DET_0} + A^{\star}_{DET_0} \; A_{DET_1}\right]\right). \tag{2.14}$$

This approximation will be assumed throughout chapter 3 and most of the rest of this work, though an instance in which it is not sufficient arises and is discussed in section 4.1.2.

2.3 The End-To-End Model

All of the formalisms described in the previous sections have been implemented in an interferometer simulation tool referred to as the "End-To-End Model," or more commonly as "E2E." E2E is a time domain simulation environment that can be used

to model a wide variety of resonant optical systems.[25] E2E was heavily used in the development and testing cycles of the lock acquisition framework presented in this work, as well as in the production of several of the figures that appear in the following chapters. However, since this work is not an exposition of modeling techniques, and the results depend in no direct way on modeling, E2E will not be discussed in detail.

Chapter 3

A Simple System: The Fabry-Perot Cavity

3.1 Optical Configuration

The simplest optical resonator, a Fabry-Perot cavity, consists of only two mirrors, but is sufficient to demonstrate many of the fundamental principals of lock acquisition. For the purpose of this discussion, the mirrors in the Fabry-Perot cavity will be assumed to be well aligned, well matched to the input beam, and to move only along the input beam axis. In this simplified scenario, lock acquisition boils down to gaining control of the relative position of the two mirrors on this axis.

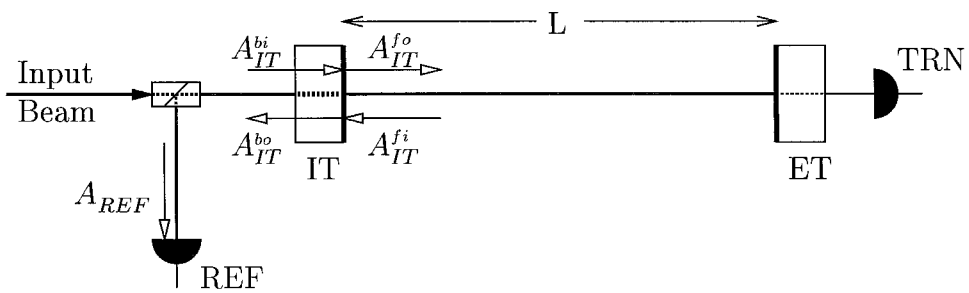

Figure 3.1: Optical layout of a Fabry-Perot cavity.

Figure 3.1 shows a model Fabry-Perot cavity system. The first component encountered by the input beam, which enters from the left, is an optical isolator. The isolator passes the input beam, but redirects the return beam to the reflection port photo-diode (REF). The Fabry-Perot cavity itself is made up of an input mirror, known in gravitation-wave research as a "test mass," and an end mirror (IT and ET). The end mirror leaks a small amount of light onto the transmission photo-diode (TRN) which is typically used to measure the power in the cavity.

There are a number of useful equations which describe the field at various points given that the mirrors move slowly (see section A.1, for derivations). The amplitude

of the intra-cavity fields, $A^{fo}_{IT_j}$, is given by

$$A^{fo}_{IT_j} = \frac{t_{IT}}{1 - r_{IT}\, r_{ET}\, e^{i\phi_j}} A^{bi}_{IT_j}, \tag{3.1}$$

where $\phi_j = 2k_j\,[L - z_{IT} - z_{ET}]$ is the round-trip phase in the cavity, and the index j refers to the frequency component of the light (see equation (2.9)). Note that the shorthand $L \equiv L_{IT:ET}$ will be used in this chapter since $L_{IT:ET}$ is the only important length in the Fabry-Perot cavity.

The reflected field, $A^{bo}_{IT_j}$, is related to $A^{fo}_{IT_j}$ by

$$A^{bo}_{IT_j} = \left[r_{IT} A^{bi}_{IT_j} - t_{IT}\, r_{ET}\, e^{i\phi_j} A^{fo}_{IT_j}\right] e^{2ik_j z_{IT}} \tag{3.2}$$

and the transmitted field, $A^{bo}_{ET_j}$, is given by

$$A^{bo}_{ET_j} = t_{ET} A^{fo}_{IT_j} e^{ik_j L}. \tag{3.3}$$

3.2 Near Resonance Control

Fabry-Perot cavities are used in gravitational-wave detectors because they can be made to increase the phase-shift of reflected light beyond that of a simple mirror. The reflected phase is most sensitive when the carrier ($j = 0$) resonates in the cavity. This resonance point is defined by

$$e^{i\phi_0} = e^{2ik_0[L+\Delta_{res}]} = 1 \tag{3.4}$$

where $\Delta = -z_{IT} - z_{ET}$ and Δ_{res} is the value of Δ at the resonance point, to be derived below.

The $z_{ET} = 0$ plane can be chosen such that $e^{2ik_0 L} = 1$, reducing equation (3.4) to

$$\Delta_{res} = n\lambda_0/2 \tag{3.5}$$

where $\lambda_j = 2\pi/k_j$ and $n \in \{0, 1, 2, 3, ...\}$. For the sake of simplicity, since all resonances are equivalent, $n = 0$, and thus $\Delta_{res} = 0$, will be assumed henceforth.

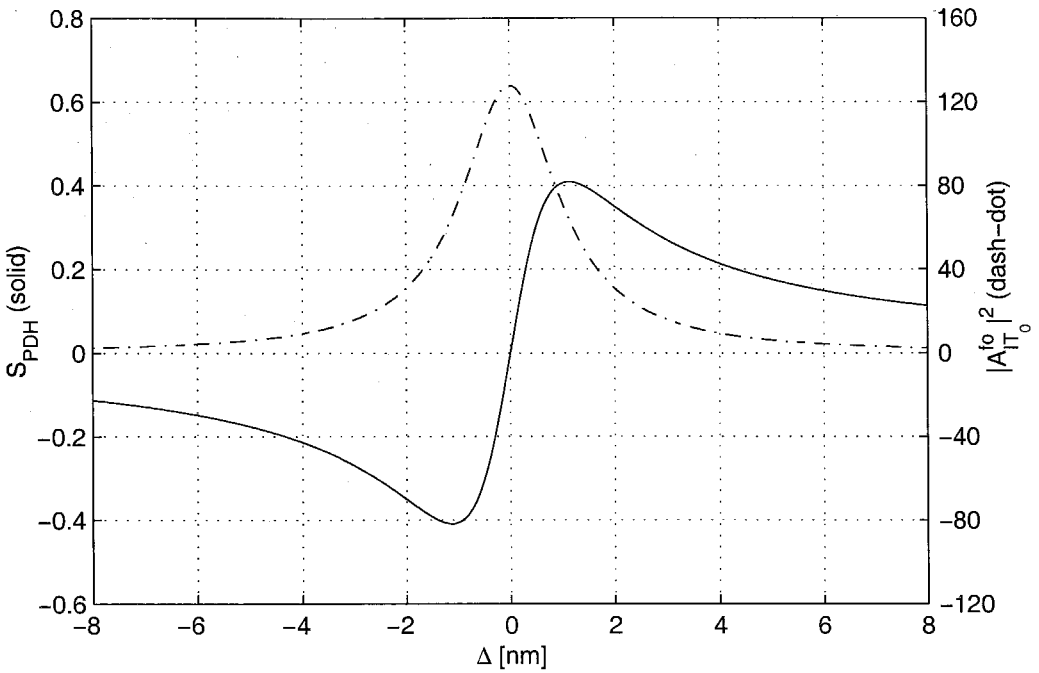

Figure 3.2: The Pound-Drever-Hall error signal for a Fabry-Perot cavity. The cavity parameters are similar to those of the LIGO 1 arm cavities. ($r_{IT} = 0.986$, $r_{ET} = 1$, and $\lambda_0 = 1064\,\text{nm}$.) The "linear region" in S_{PDH} is centered at $\Delta = 0$ and approximately 1 nm wide. In this region a standard linear controller can be used to hold the cavity on resonance. The carrier power in the cavity, $\left|A^{fo}_{IT_0}\right|^2$, is also shown for reference. Note that the key is given along with the axis labels.

Given that $\Gamma_{mod} < 1$, so that equation (2.14) can be used, the demod signal at the reflection port is

$$S_{demod} = \mathcal{I}m\left(e^{i\phi_{demod}}\left[A^{\star}_{REF_{-1}}\, A_{REF_0} + A^{\star}_{REF_0}\, A_{REF_1}\right]\right). \tag{3.6}$$

Further assuming that L and ω_{mod} have been chosen such that the first-order sidebands ($j \in \{-1, 1\}$) are far from resonance when the carrier is resonant (i.e., such

that $A^{bo}_{IT_1} \simeq -A^{bo}_{IT_{-1}} \simeq A^{bi}_{IT_1} e^{2ik_j z_{IT}}$), and that $\phi_{demod} = 0$,

$$S_{demod} \simeq 2\,\mathcal{I}m\left(A^{\star}_{REF_0}\, A_{REF_1}\right) \tag{3.7}$$

$$\simeq 2t^2_{REF}\,\mathcal{I}m\left(A^{bi}_{IT_1} A^{bo\,\star}_{IT_0}\right) \tag{3.8}$$

where $t_{REF} \equiv A_{REF_j}/A^{bo}_{IT_j}$ is the transmissivity of the optical train leading to the reflection port photodetector. Finally, combining this result with equations (3.1) and (3.2) yields the error signal for "Pound-Drever-Hall reflection locking,"

$$S_{PDH} = 2t^2_{REF}\,\mathcal{I}m\left(A^{bi}_{IT_1}\, A^{bi\,\star}_{IT_0}\left[r_{IT} - \frac{t^2_{IT}\, r_{ET}\, e^{i\phi_0}}{1 - r_{IT}\, r_{ET}\, e^{i\phi_0}}\right]^{\star}\right). \tag{3.9}$$

Making the substitution $A^{bi}_{IT_j} \rightarrow A_{IN}\; J_j(\Gamma_{mod})$ from equation (2.9) leads to

$$S_{PDH} = -2t^2_{REF}\,|A_{IN}|^2\; J_0(\Gamma_{mod})\; J_1(\Gamma_{mod})\; \mathcal{I}m\left(r_{IT} - \frac{t^2_{IT} r_{ET} e^{i\phi_0}}{1 - r_{IT} r_{ET} e^{i\phi_0}}\right) \tag{3.10}$$

$$= 2\,|A_{IN}|^2\; J_0(\Gamma_{mod})\; J_1(\Gamma_{mod})\, \frac{t^2_{REF}\; r_{ET}\; t^2_{IT}}{\left|1 - r_{IT}\; r_{ET}\; e^{i\phi_0}\right|^2} \sin(2k_0\Delta) \tag{3.11}$$

$$= 2t^2_{REF}\; r_{ET}\; \left|A^{fo}_{IT_0}\right|^2 \frac{J_0(\Gamma_{mod})}{J_1(\Gamma_{mod})} \sin(2k_0\Delta) \tag{3.12}$$

where the last step utilizes equation (3.1). In the region where S_{PDH} is proportional to Δ (henceforth the "linear region," see figure 3.2) linear control theory can be applied and a controller that will hold the cavity on resonance is easily derived. The width of this region is approximately $\lambda_0/4\mathcal{F}$, where

$$\mathcal{F} = \frac{\pi\sqrt{r_{IT}\; r_{ET}}}{1 - r_{IT}\; r_{ET}} \tag{3.13}$$

is the finesse of the cavity.

This technique is the foundation for the control schemes used in all ground-based interferometric gravitational-wave detectors. However, unless it is possible to set $|\Delta| < \lambda_0/4\mathcal{F}$ in the absence of a control loop, use of S_{PDH} (and S_{demod} in general) brings forth the problem of how one arrives in the linear region. This is the essence of the lock acquisition problem.

3.3 Lock Acquisition Threshold Velocity

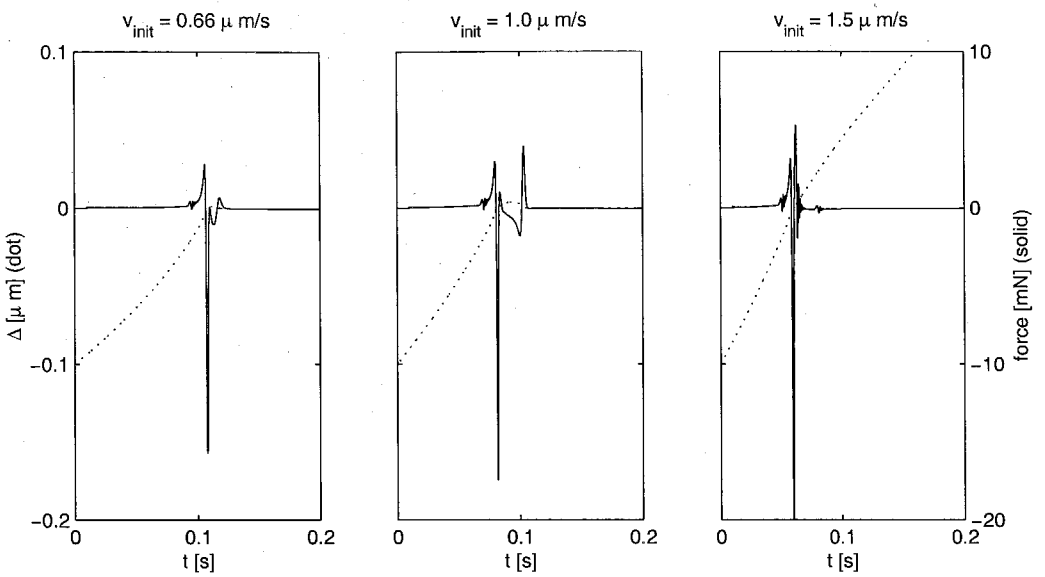

Figure 3.3: Threshold velocity in a simple lock acquisition model. A linear controller attempts to lock the cavity as $\Delta = 0$ is approached with various initial velocities v_{init}. From left to right, the first is well below the threshold velocity, the second just below, and the third well above.

Attempts to be quantitative about the effectiveness of various lock acquisition schemes lead to the definition of the "threshold velocity" of a given scheme as the value of $\left|\frac{d\Delta}{dt}\right|$ below which the controller will "acquire" and hold a cavity near resonance.[15] Threshold velocity is a useful measure of effectiveness only in cavities where $\frac{d\Delta}{dt}$ can be thought of as a constant over time periods shorter than the time required to cross the resonance ($\sim \frac{\lambda_0}{\mathcal{F}\left|\frac{d\Delta}{dt}\right|}$) since it implicitly assumes that in the absence of the controller $\frac{d\Delta}{dt}$ would have remained constant.[1]

When attempting to determine the threshold velocity for a control scheme, it is important to keep the limitations of the actuation system in mind. The actuation model considered here is that of a force applied directly to the optic. Other actuation systems will have additional subtleties, but all systems are likely to, in the end,

[1]The optics in LIGO and other detectors are suspended to provide seismic isolation at high frequencies. Furthermore, seismic motion is largest at low frequencies (~ 0.1 Hz), and, as a result, Δ is typically dominated by low frequency motion of the suspended optics. This makes threshold velocity a meaningful quantity in these systems.

accelerate the optics via some force. The only limitation that will be assumed is that of a maximum actuation force.

The phase of the input field can also be used as a form of actuation. While this can be very effective in systems involving only one long base-line resonant cavity, systems which involve multiple cavities (e.g., any of the resonant detector configurations discussed in chapter 1) can only use this technique to actuate one degree of freedom.

3.4 Simple Lock Acquisition

The approach to lock acquisition first and most often taken is to enable the control scheme designed to work in the linear region and wait for lock to be acquired.[22, 13, 23] This approach is beautiful in its simplicity, and can work well for the Fabry-Perot cavity, but is not effective when dealing with complex interferometers. The threshold velocity for this type of scheme depends on the details of the controller and the interferometer, but there are some features that all such schemes have in common.

The primary problem with applying a linear controller that uses S_{demod} as its error signal to lock acquisition is that the controller inevitably behaves badly away from the linear region. Figure 3.3 shows example fringe crossings above and below a typical linear controller's threshold. Notice that the controller increases $\left|\frac{d\Delta}{dt}\right|$ as the linear region is approached, thereby making the problem of stopping the optics involved more difficult. Near the threshold velocity, success is only achieved by virtue of a large force applied as the linear region is crossed. Realistic actuation limits considerably reduce the threshold velocity of this type of controller (see figure 3.4).

3.5 Guided Lock Acquisition

One approach to increasing the threshold velocity of a linear controller is to pair it with a non-linear controller. The non-linear controller is used to lower $\left|\frac{d\Delta}{dt}\right|$ until it is less than the threshold velocity for the associated linear controller.

The scheme described by Camp et al., dubbed "guided lock acquisition," and

similar schemes,[15, 1] attempt to estimate $\frac{d\Delta}{dt}$ by analyzing the signals observed as Δ crosses zero (see section A.2.) Given a velocity estimate, control forces can be applied such that Δ returns to zero with a lower value of $\left|\frac{d\Delta}{dt}\right|$ than in the previous crossing. Under the assumptions that define threshold velocity (the frequency of the input field, ω_0, is constant and no forces other than the control forces are applied to the optics), these schemes work quite well. In real interferometers, however, these assumptions are violated. The "error" associated with the violation of these assumptions, integrated over the time required to return to $\Delta = 0$, limits the effectiveness of this approach.

These schemes suffer somewhat from their inherent complexity, and are difficult to generalize to complex systems in which robust velocity estimation is more challenging. This work seeks a more general solution to the problem of lock acquisition. The idea of guided lock acquisition is presented here for completeness and because in some noise environments it may be an appropriate addition to a more general scheme.

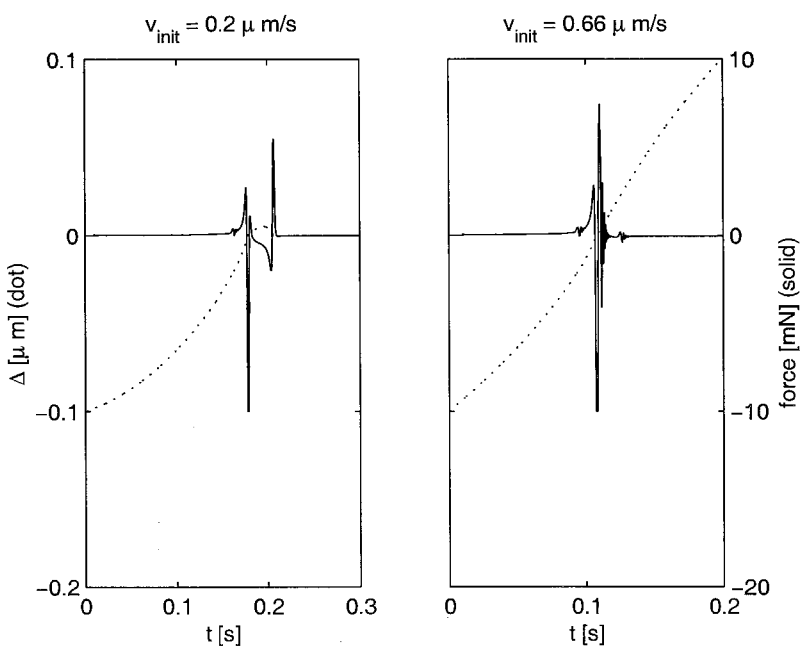

Figure 3.4: Threshold velocity in a more realistic lock acquisition model. Including realistic actuation limits significantly reduces the threshold velocity of a linear controller. The model parameters are taken from the LIGO 1 arm cavity: the force limit is 10 mN and the mass of the optic is 10.3 kg.

3.6 Error Signal Linearization

A second approach to increasing the threshold velocity of a linear controller is to combine signals so as to increase the width of the linear region, thereby making the linear controller more effective. In a Fabry-Perot cavity, a simple combination of power and demod signals can be used to produce an error signal with a broad linear region (see figure 3.5)

$$S_{Lin} \equiv \frac{S_{PDH}}{P_{TRN}} \tag{3.14}$$

$$= \frac{S_{PDH}}{\sum_j \left| t_{ET} A^{fo}_{IT_j} \right|^2} \tag{3.15}$$

where P_{TRN} is the power incident on the TRN detector. Since the interesting region is near the carrier resonance, and far from the sideband resonances, $P_{TRN} \simeq \left| t_{ET} A^{fo}_{IT_0} \right|^2$ can be used in combination with equation (3.12) to simplify equation (3.15)

$$S_{Lin} \simeq \frac{S_{PDH}}{\left| t_{ET} A^{fo}_{IT_0} \right|^2} \tag{3.16}$$

$$\simeq 2 \frac{r_{ET} t^2_{REF}}{t^2_{ET}} \frac{J_1(\Gamma_{mod})}{J_0(\Gamma_{mod})} \sin(2k_0\Delta) \,. \tag{3.17}$$

The most significant limitations to the threshold velocity achievable with error signal linearization arise from noise in P_{TRN} and the breakdown of the assumptions that go into equation (3.17) away from $\Delta \sim 0$ (e.g., when a sideband resonance is encountered). While the first of these is not an issue in simulation, a typical experimental setup may require $P_{TRN} > 0.1 P_{TRN}|_{\Delta=0}$ before enabling the cavity control loop. (See figure 3.6.) These limitations assure that, for cavities with $\mathcal{F} \gg 1$, the useful region of S_{Lin} satisfies $|k_0\Delta| \ll \pi$ and equation (3.17) can be simplified to

$$S_{Lin} \simeq 4k_0 \frac{r_{ET} t^2_{REF}}{t^2_{ET}} \frac{J_1(\Gamma_{mod})}{J_0(\Gamma_{mod})} \Delta. \tag{3.18}$$

Error signal linearization has been tested experimentally with the 2 kilometer-long cavities at the LIGO Hanford Observatory and the 4 kilometer cavities at the LIGO

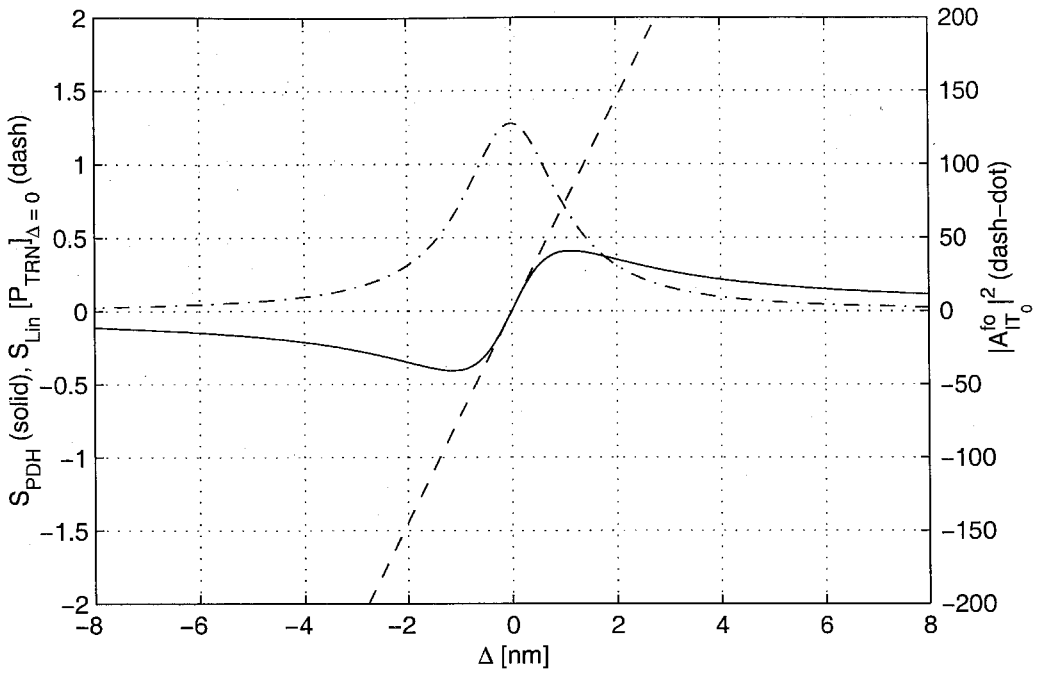

Figure 3.5: Error Signal Linearization. S_{Lin} is scaled by P_{TRN} at $\Delta = 0$ such that the slopes of S_{Lin} and S_{PDH} are equal near the resonance point and $\left|A^{fo}_{IT_0}\right|^2 = P_{TRN}/t^2_{ET}$ is shown for reference. The broad linear region in S_{Lin} makes it a superior error signal for use with a linear controller, especially during lock acquisition.

Livingston Observatory (see section 5.1.1 for details about the interferometers). This technique was observed to significantly improve the lock acquisition performance of a cavity over that of a simple linear control loop at both sites.

The threshold velocity of the lock acquisition system at the Hanford observatory was measured to be $1 \pm 0.1\,\mu$m/ s. This measurement was made by exciting one of the mirrors, then enabling the lock acquisition system. The lowest velocity resonance crossed without locking sets an upper limit on the threshold velocity of the controller, and the highest velocity capture sets a lower limit. In some cases, a lock event very near the threshold occurs (see figure 3.7), producing tight bounds. A similar method was applied to measuring the threshold velocity of a simple linear controller applied to the same cavity. The accelerations produced by this "always on" controller make bounding the threshold velocity more difficult, but missed resonance crossings indicate a loose upper bound of $0.65\,\mu$m/ s.

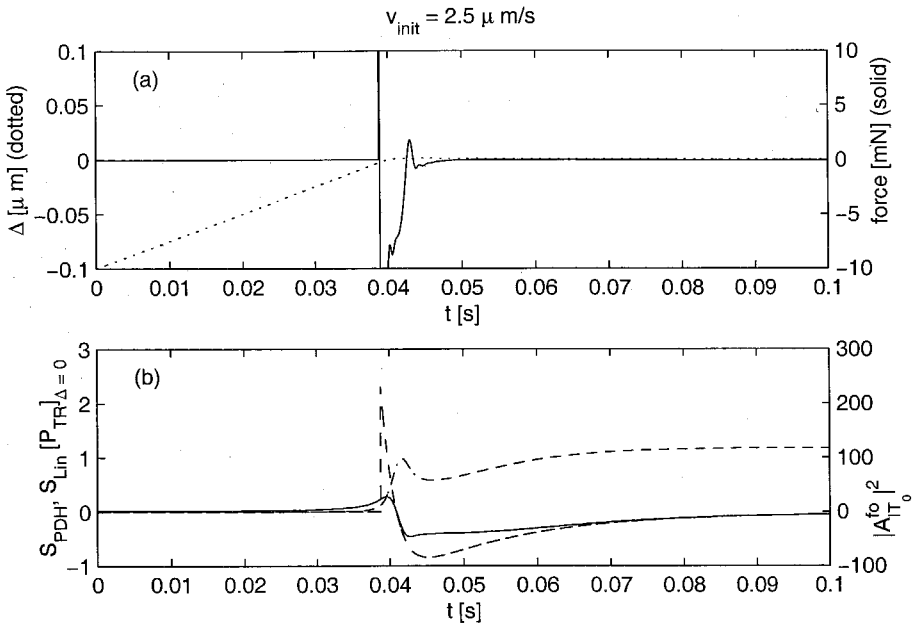

Figure 3.6: Threshold velocity with error signal linearization, simulated. Figure (a) shows Δ and the force applied to the corresponding degree of freedom during a simulated lock acquisition event. The power in the cavity ($\left|A^{fo}_{IT_0}\right|^2$, dash-dot), demod signal (S_{demod}, solid), and linearized error signal (S_{Lin}, dashed) are shown in (b) for the same event. The error signal used for locking is enabled as P_{TRN} crosses 10% of its peak value; this is the point at which S_{Lin}, as shown above, becomes non-zero (just before $t = 0.04$). Note that the threshold velocity of this controller is more than ten times greater than that shown in figure 3.4 for a controller without error signal linearization, despite having identical actuation limitations.

Error signal linearization has proven to be a robust and effective technique for lock acquisition in a Fabry-Perot cavity. An equally important feature of this technique is its generalizability to more complex systems, which is the topic of the next chapter.

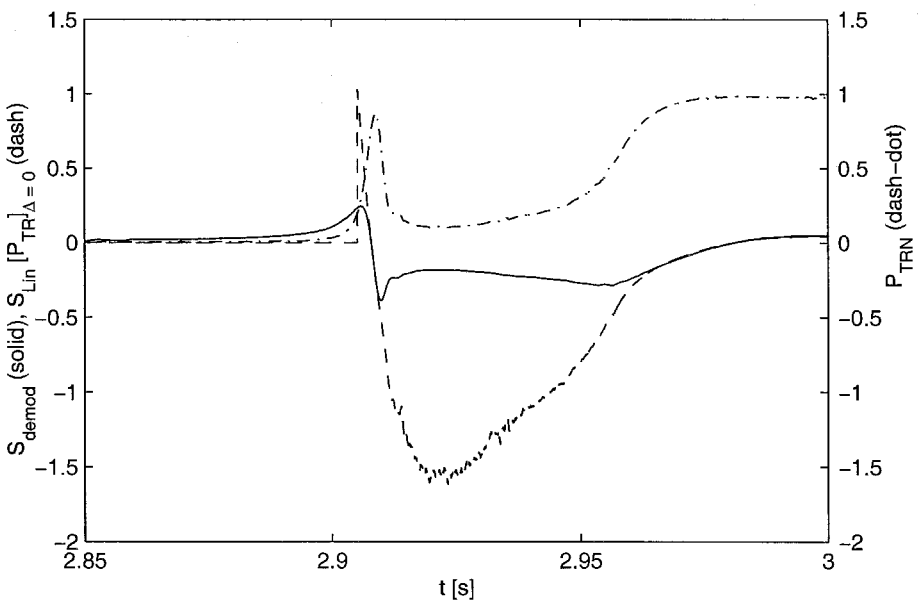

Figure 3.7: Threshold velocity with error signal linearization, experimental. These data were collected at the LIGO Hanford Observatory using one of the 2 km arm cavities. This event, which has $v_{init} \sim 1\,\mu$m/ s, is very near the threshold velocity of the controller. Note how S_{Lin} continues to grow even after the linear region in S_{demod} has been crossed, thereby allowing the controller to acquire lock when it would have otherwise been lost.

Chapter 4

Complex Resonant Systems

This chapter is a general discussion of lock acquisition in complex systems, with the power recycled LIGO 1 optical configuration, discussed in section 4.1.2, serving as the canonical example. The approach is to generalize "Error Signal Linearization," discussed in the previous chapter, to interferometers with multiple degrees of freedom.

The objective of a lock acquisition system is to take the interferometer from an uncontrolled state to its operating point, and hold it there. This progression will generally follow a well defined path along which the interferometer's control loops are sequentially engaged and the associated degrees of freedom are "locked" to their operating points. In the course of lock acquisition, the fields in the interferometer change and the response of its outputs change accordingly. The lock acquisition system must compensate for these changes so as to maintain the stability of the active control loops, and allow for the activation of the remaining loops.

4.1 The Sensing Matrix

The first step in controlling an interferometer is understanding the relationship between the demodulated outputs and the interferometer's degrees of freedom. The "sensing matrix" or "matrix of discriminants," $\mathbf{M}$, represents this relationship as the solution to

$$\vec{S}_{demod} = \mathbf{M}\vec{\Delta}. \tag{4.1}$$

Historically, the sensing matrix has been used only to express the time independent linear components of this relationship at an interferometer's operating point.[18, 22] For the purpose of lock acquisition, the use of the sensing matrix must be expanded somewhat to include the dependence of the matrix elements on the fields in the

interferometer.

In this context the sensing matrix is a continuously evolving entity which the lock acquisition system must estimate with sufficient accuracy to obtain and maintain control of the interferometer. It should be noted that, despite its non-static nature, the sensing matrix does not attempt to account for high-velocity cavity dynamics (see section A.2.) Furthermore, the discussion of frequency dependence in the sensing matrix will be forestalled until section 4.4.

Determining a useful expression for $\mathbf{M}$ in general is an extremely difficult task, but a common special case occurs for most demod signals. In this special case a matrix element is given by a sum of terms of the form

$$\mathbf{M}_{p,q} = \sum g_m \frac{\left|A_{CAV_m}\right|^2}{A_{INC_m}} A_{LO_l} \tag{4.2}$$

where A_{CAV_m} is an intra-cavity field, A_{INC_m} is the input field for the cavity, A_{LO_l} is a field at the detector, g_m is a constant gain factor and $|l - m| = 1$.

Equation (4.2) can be understood intuitively as a collection of gain factors applied to a disturbance[1] generated by changing $\vec{\Delta}_q$. The initial amplitude of the disturbance is proportional to the amplitude of the resonant field from which it originates, A_{CAV_m}. A sufficiently low frequency disturbance experiences the same gain in the cavity of its origin as its parent field, A_{CAV_m}/A_{INC_m}. g_m is the gain factor which takes the disturbance from that cavity to the photo-detector that produces S_{demod_p}, where a signal is generated by its interaction with the field A_{LO_l}, known as the "local oscillator." Equation (4.2) is simply the product of these factors, summed over all resonant field-local oscillator pairs.

In the following sections this rather obtuse description is applied to the Fabry-Perot cavity and the LIGO 1 configuration. The sensing matrix for a Fabry-Perot cavity is derived from the discussion in chapter 3 and a practical implementation is briefly discussed. The LIGO 1 sensing matrix is presented, but the details of its

[1]This "disturbance" can be quantified through the formalism of "audio sidebands" as presented in chapter 3 of [21].

implementation are not discussed until chapter 5.

4.1.1 Fabry-Perot Cavity Sensing Matrix

In the case of the Fabry-Perot cavity discussed in chapter 3, the sensing matrix

$$\mathbf{M}_{FP} = \left[\!\!\left[\; 4k_0 t_{REF}^2 r_{ET} \, \frac{A_{IT_1}^{bi}}{A_{IT_0}^{bi}} \left| A_{IT_0}^{fo} \right|^2 \; \right]\!\!\right] \tag{4.3}$$

is simply the linear coefficient of Δ in equation (3.12). To clarify the relationship between this equation and equation (4.2), note that there are two terms in the sum, both with $m = 0$,

$$\begin{aligned} A_{CAV_0} &= A_{IT_0}^{fo} \\ A_{INC_0} &= A_{IT_0}^{bi} \\ g_0 &= 2k_0 t_{REF}^2 r_{ET}, \end{aligned}$$

but with different local oscillators

$$\begin{aligned} A_{LO_1} &= A_{IT_1}^{bo} \\ A_{LO_{-1}} &= -A_{IT_{-1}}^{bo}. \end{aligned}$$

Since $A_{IT_1}^{bo} = -A_{IT_{-1}}^{bo} \simeq A_{IT_1}^{bi}$ is assumed (see text preceding equation (3.7)), these two terms are combined in equation (4.3). In practice, equation (4.3) is reduced to

$$\mathbf{M}_{FP} = \left[\!\!\left[\; g_{FP} \; P_{TRN} \; \right]\!\!\right] \tag{4.4}$$

where $P_{TRN} \simeq \left| t_{ET} A_{IT_0}^{fo} \right|^2$ is measured in real-time, and g_{FP} is an empirically determined gain factor that includes the details of the detection electronics as well as the optical properties of the cavity.

4.1.2 LIGO 1 Sensing Matrix

The considerable support structure aside, the LIGO 1 interferometers consist of 6 mirrors and 5 photo-detectors. The Michelson cornerstone is formed by the beam-splitter (BS) and the two input mirrors (IT on the "transmitted side" of the BS, and IR on the "reflected side"). The input mirrors transmit about 3% of the light incident on them into the cavities they form with the end mirrors (ET and ER). Finally, the power recycling mirror (PR) serves to increase the power in the interferometer by "recycling" the light that would otherwise be dumped at the reflection port.

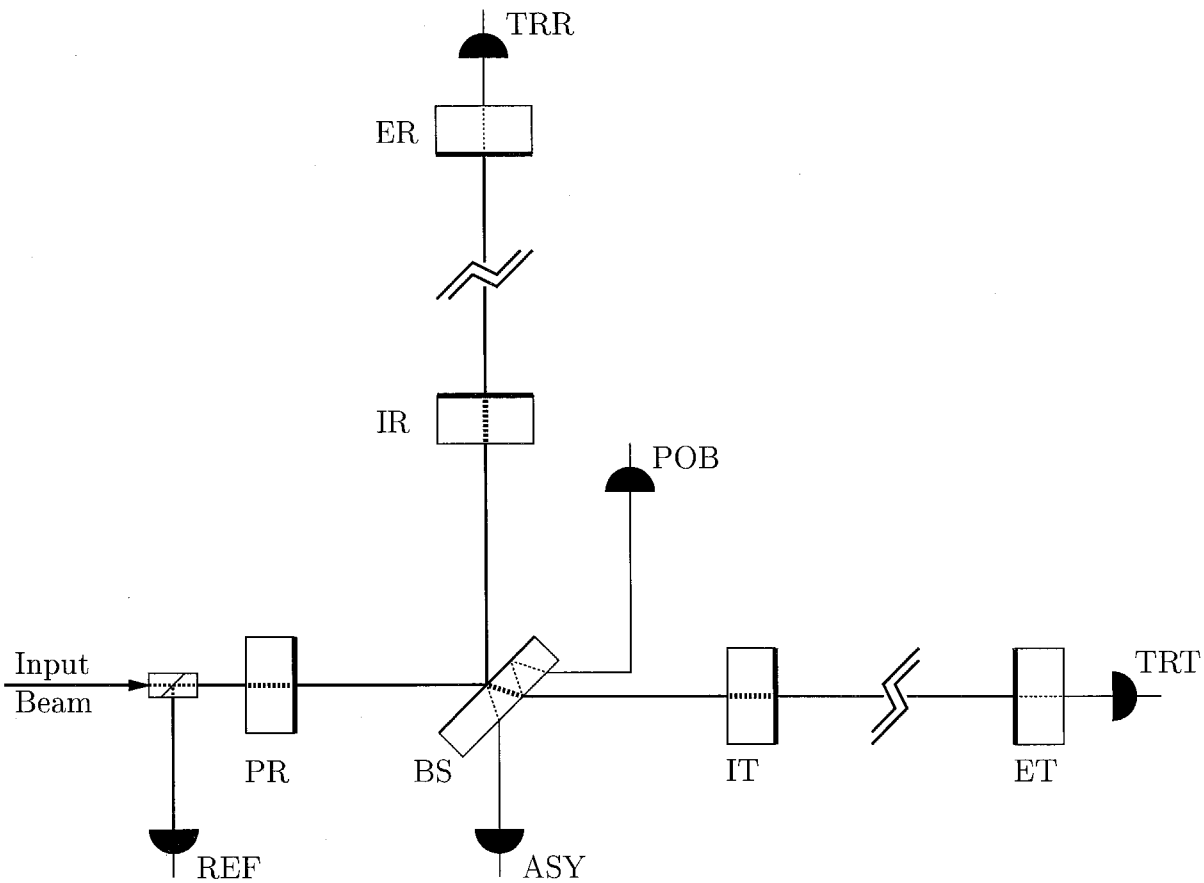

Figure 4.1: LIGO 1 optical layout.

The three sensors in and around the power recycling cavity all produce both demod signals and DC power signals. The reflection port sensor (REF) detects the light that returns from the interferometer. This light is made up of the promptly reflected

field, and the leakage field (i.e., the field that leaks out of the interferometer through the PR). The antisymmetric port sensor (ASY) is very sensitive to antisymmetric changes in the length of the arms (e.g., gravitational waves), which cause light to leak out this port. The beam-splitter pick-off (POB) samples the light incident on the beam-splitter (from the PR) and provides information about the fields in the power recycling cavity. Lastly, the transmission monitors (TRT and TRR) produce DC power signals that are used to monitor the power in the arm cavities. (See chapter 5 for more detailed information about the LIGO 1 interferometers.)

Power-recycled interferometers, and the LIGO 1 interferometers in particular, have four longitudinal degrees of freedom,

$$\vec{\Delta} = \begin{bmatrix} \Delta_{cArm} \\ \Delta_{dArm} \\ \Delta_{PRC} \\ \Delta_{Mich} \end{bmatrix} = \begin{bmatrix} -[z_{IT} + z_{ET} + z_{IR} + z_{ER}] \\ z_{IR} + z_{ER} - [z_{IT} + z_{ET}] \\ z_{IT} + z_{IR} - z_{BS}/\sqrt{2} - z_{PR} \\ z_{IT} - z_{IR} + z_{BS}/\sqrt{2} \end{bmatrix}, \tag{4.5}$$

which represent the common and differential mode deviations of the arms from resonance (cArm and dArm), the deviation of the power-recycling cavity length from resonance (PRC), and the deviation of the Michelson from a dark-fringe (Mich). The LIGO 1 interferometer design offers five demod signals with which to control these degrees of freedom,

$$\vec{S}_{demod} = \begin{bmatrix} I_{ref} \\ I_{pob} \\ Q_{asy} \\ Q_{ref} \\ Q_{pob}, \end{bmatrix} \tag{4.6}$$

where "I" (In-Phase) and "Q" (Quad-Phase) are orthogonal demodulation phases. Note that for the purpose of controlling a power-recycled interferometer, there is only one useful signal at the ASY port. The label assigned to this signal's demodulation phase is arbitrary, but despite the fact that this signal has properties similar to the

in-phase signals at other ports, and dissimilar to the quad-phase signals, it is referred to as Q_{asy}. I_{asy} does not appear in the demod signal vector.

The dominant elements of the sensing matrix for a LIGO 1 interferometer are[2]

$$G_{cArm,I_{ref}} = g_{Aref}\ A_{REF_1}\ A_{+} \tag{4.7}$$

$$G_{dArm,I_{ref}} = g_{Aref}\ A_{REF_1}\ A_{-} \tag{4.8}$$

$$G_{PRC,I_{ref}} = g_{Pref}\ \left[A_{REF_0} - A_{REF_2}\right]\ A_{PRM} \tag{4.9}$$

$$G_{cArm,I_{pob}} = g_{Apob}\ A_{POB_1}\ A_{+} \tag{4.10}$$

$$G_{dArm,I_{pob}} = g_{Apob}\ A_{POB_1}\ A_{-} \tag{4.11}$$

$$G_{PRC,I_{pob}} = g_{Ppob}\ A_{POB_0}\ A_{PRM} \tag{4.12}$$

$$G_{cArm,Q_{asy}} = g_{Aasy}\ A_{ASY_1}\ A_{-} \tag{4.13}$$

$$G_{dArm,Q_{asy}} = g_{Aasy}\ A_{ASY_1}\ A_{+} \tag{4.14}$$

$$G_{Mich,Q_{ref}} = g_{Mref}\ \left[A_{REF_0} + A_{REF_2}\right]\ A_{PRM} \tag{4.15}$$

$$G_{Mich,Q_{pob}} = g_{Mpob}\ A_{POB_0}\ A_{PRM} \tag{4.16}$$

where

$$A_{\pm} = \frac{\left|A^{fo}_{IT_0}\right|^2 \pm \left|A^{fo}_{IR_0}\right|^2}{A^{fo}_{PR_0}}, \tag{4.17}$$

$$A_{PRM} = \frac{\left|A^{fo}_{PR_1}\right|^2}{A^{bi}_{PR_1}}, \tag{4.18}$$

and the various gs are constant gain coefficients. These equations are all of the form shown in (4.2) and many can be derived from the steady state signal responses.[26] The contribution from the second-order sidebands has been included only in the reflected signals since, while carrier contribution dominates at other ports, A_{REF_0} may go to zero, making A_{REF_2} the dominant contributor to the reflected signal.

Filling in zeros for the (relatively small) elements of the sensing matrix not given

[2]These equations assume that $r_{IT} = r_{IR}$, $t_{IT} = t_{IR}$, and $r_{BS} = t_{BS} = \frac{1}{\sqrt{2}}$. They also assume that $A_{X_j} \simeq -A_{X_{-j}}$, which, while not true in general, is satisfied in all regions of interferometer state space that are relevant to this discussion. None of these assumptions are necessary to the workings of the formalism presented here, but they considerably simplify the associated mathematical expressions and do not hinder the development of a functional lock acquisition scheme.

above yields the full sensing matrix,

$$\mathbf{M}_{PR} = \begin{bmatrix} G_{cArm,I_{ref}} & G_{dArm,I_{ref}} & G_{PRC,I_{ref}} & 0 \\ G_{cArm,I_{pob}} & G_{dArm,I_{pob}} & G_{PRC,I_{pob}} & 0 \\ G_{cArm,Q_{asy}} & G_{dArm,Q_{asy}} & 0 & 0 \\ 0 & 0 & 0 & G_{Mich,Q_{ref}} \\ 0 & 0 & 0 & G_{Mich,Q_{pob}} \end{bmatrix}. \tag{4.19}$$

4.2 The Input Matrix

The "input matrix" is the matrix that is needed to produce error signals for an interferometer's degrees of freedom given its demodulated output. Ideally, the input matrix solves the equation

$$\vec{\Delta} \simeq \mathbf{G}\vec{S}_{demod} \tag{4.20}$$

and is simply the inverse of the sensing matrix, but there are a number of things that complicate this relationship.

The most immediate complication is that $\mathbf{M}$ is not necessarily a square matrix. In order for an interferometer to be controllable, the number of demodulated signals must be greater than or equal to the number of degrees of freedom. If there are more demodulated signals than degrees of freedom, there will be an infinite set of solutions to equation (4.20) from which the system designer may choose.

An example of this type of complication can be seen in $\mathbf{M}_{PR}$ above. The solution in this case is to eliminate one of the two quad-phase signals that provide information about Δ_{Mich}. The choice of which to remove is made dynamically based on noise considerations and is discussed in section 5.1.

A more significant complication arises from singularities in $\mathbf{M}$. There are two fundamentally different types of singularities: "no signal" and "degenerate signal" singularities. Singularities effectively reduce the number of demod signals, thereby rendering one or more of the interferometer's degrees of freedom uncontrollable.

The general algorithm for handling singularities in $\mathbf{M}$ is as follows:

1. Remove rows and columns from $\mathbf{M}$ until the remaining matrix, $\tilde{\mathbf{M}}$, is invertible.
2. For each row and column removed from $\mathbf{M}$ to produce $\tilde{\mathbf{M}}$, set the corresponding columns and rows of $\mathbf{G}$ to zero.
3. Invert $\tilde{\mathbf{M}}$ to produce the remaining elements of $\mathbf{G}$.

The input matrix produced by this algorithm solves the equation

$$\vec{S}_{err} = \mathbf{G}\vec{S}_{demod} \tag{4.21}$$

where $\vec{S}_{err_p} \simeq \vec{\Delta}_p$ for the rows of $\mathbf{G}$ not eliminated in step 2, and $\vec{S}_{err_p} = 0$ otherwise.

4.2.1 No Signal Singularities

No signal (NS) singularities occur when a matrix element becomes so small that it is dominated by noise in the measurement of its constituents. This situation is handled by the setting the offending matrix element to zero. These zeros may cause the sensing matrix to become singular and while this represents a lack of information rather than a true singularity, the result is the same.

The Fabry-Perot cavity offers a simple example of an NS singularity. When the cavity is far from resonant (i.e., $|\Delta| \gg \lambda_0/\mathcal{F}$), P_{TR} becomes small and its measured value is bound to be dominated by noise and other effects. In this situation S_{demod} offers little information about Δ and it cannot be used to generate meaningful control forces, so $\mathbf{G}_{FP} = \mathbf{0}$ is used. The discontinuity resulting from the removal of this NS singularity can be seen in figure 3.6 as a jump in the linearized error signal from 0 to 2.2 just before $t = 0.04$.

The explicit zeros present in $\mathbf{M}_{PR}$ are also of this origin. It is true, of course, that in a real interferometer no element of $\vec{S}_{demod}$ is totally insensitive to any element of $\vec{\Delta}$, but the elements that are small or indeterminant are set to zero by the "no signal rule" described above.

4.2.2 Degenerate Signal Singularities

Degenerate signal (DS) singularities arise when two demod signals become linearly dependent (i.e., two signals contain the same information). This is a true matrix singularity that can occur while the power in the interferometer is changing.

Since the estimation of the sensing matrix is imperfect, the region around a DS singularity must be handled with care. As the matrix determinant goes to zero the elements of $\mathbf{G}$ become large and imperfections in $\mathbf{M}$ and $\vec{S}_{demod}$ (e.g., small DC offsets) will cause control to be lost. For this reason, the notion of matrix "singularity" must be broadened somewhat. A sensing matrix is considered singular if the absolute value of the normalized determinant (see appendix B.3) is less than some predetermined minimum, typically about 0.1.

4.3 Multi-Step Lock Acquisition

The general process of lock acquisition can be described as the expansion of the invertible part of the sensing matrix, $\tilde{\mathbf{M}}$, accomplished by the removal of NS singularities from $\mathbf{M}$. The process begins with $\tilde{\mathbf{M}}$ of minimal dimension, and ends when $\tilde{\mathbf{M}}$ is stable and has the same dimensionality as $\mathbf{G}$. In order for lock acquisition to occur there must be a path from the uncontrolled state to the fully controlled state along which $\mathbf{G}$ can be determined with sufficient accuracy to maintain control.

The particulars of the lock acquisition path depend on the interferometer in question and the signals it makes available. The following sections outline the lock acquisition path for a LIGO 1 interferometer.

4.3.1 State 1

None of the degrees of freedom are controlled. The cavities occasionally resonate as the mirrors move freely. This is the starting point for lock acquisition.

In this state $\mathbf{G} = \mathbf{0}$ and $\tilde{\mathbf{M}}$ is a 0 by 0 matrix.

4.3.2 State 2

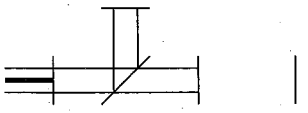

Δ_{Mich} and Δ_{PRC} are controlled such that the carrier is anti-resonant in the power recycling cavity and zero at the ASY port. The recycling cavity length and the modulation frequency are chosen such that the carrier anti-resonance is coincident with a resonance for the first-order sidebands.[3] The sideband power in the recycling cavity in this state, and throughout the rest of the state progression, is about ten times the input sideband power. There is essentially no carrier power in the interferometer in this state.

In state 2 $\tilde{\mathbf{M}}$ becomes the 2 by 2 matrix

$$\tilde{\mathbf{M}}_{PR_2} = \begin{bmatrix} G_{PRC,I_{ref}} & 0 \\ 0 & G_{Mich,Q_{ref}} \end{bmatrix}$$

which uses I_{ref} and Q_{ref} to produce error signals for Δ_{PRC} and Δ_{Mich}.

4.3.3 State 3

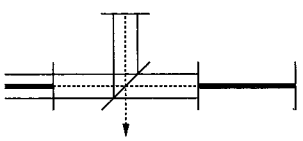

State 3 is reached when state 2 holds and one of the two arm cavities is controlled such that the carrier is resonant. Resonance in the arm cavity causes the carrier field reflected from that arm to reverse its sign, thereby making the ASY port bright for the carrier. This sign reversal results from the over-coupled nature of the arm cavity (i.e., $r_{IT} < r_{ET}$) and has a number of beneficial properties which are beyond the scope of this work.

With an arm cavity resonant, the carrier power in that arm increases to approximately four times that of the input beam. The carrier field in the arm can now be used to sense its length, thereby removing a NS singularity from $\mathbf{M}$ and expanding

[3] This requirement can be expressed as $2L_{PR:BS} + L_{BS:IT} + L_{BS:IR} = (n + \frac{1}{2})\lambda_{mod}$, where $\lambda_{mod} = 2\pi c/\omega_{mod}$ is the modulation wavelength and $n \in \{0, 1, 2, 3, ...\}$.

$\tilde{\mathbf{M}}$ to

$$\tilde{\mathbf{M}}_{PR_3} = \begin{bmatrix} G_{cArm,I_{ref}} & G_{PRC,I_{ref}} & 0 \\ G_{cArm,Q_{asy}} & 0 & 0 \\ 0 & 0 & G_{Mich,Q_{ref}} \end{bmatrix}.$$

Note that in this state $\Delta_{dArm} = \pm\Delta_{cArm}$, depending on which arm is locked.

4.3.4 State 4

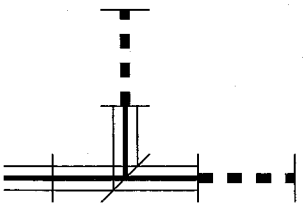

This is a transitory state that occurs when state 3 holds and the as yet uncontrolled arm cavity is locked at carrier resonance. In this state the carrier is resonant in both arm cavities and the recycling cavity. The resulting coupled cavity allows the carrier power in the interferometer to increase by roughly three orders of magnitude.

At the onset of this state all of the degrees of freedom are controlled and all of the NS singularities have been removed from $\mathbf{M}$. A DS singularity is, however, encountered in the course of the power buildup. As the singularity is approached, control of Δ_{PRC} is relinquished, but is regained once the DS singularity is passed enroute to state 5.

4.3.5 State 5

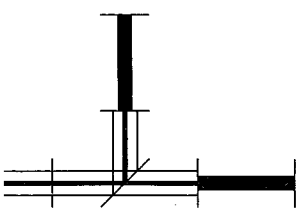

The final state of the interferometer, at least from the lock acquisition point of view, is reached when state 4 has endured long enough for the power in the interferometer to stabilize. This is the ending point for lock acquisition, though the controllers used to achieve this state must be capable of holding it long enough for the transition to a low-noise controller to occur.

The lock acquisition path for the LIGO 1 configuration was first described by Lisa Sievers, though she did not include state 5. State 5 is used to distinguish between the point at which all degrees of freedom are controlled, state 4, and the point at which stable lock has been achieved. The time between acquisition of state 4 and acquisition

of state 5 for the LIGO 1 interferometers is of order a half-second (see figure 4.2). The distinction between these two states is important because, as a result of the DS singularity and the large increase in circulating power that occur during this time, maintaining control of the interferometer during state 4 can be quite challenging.

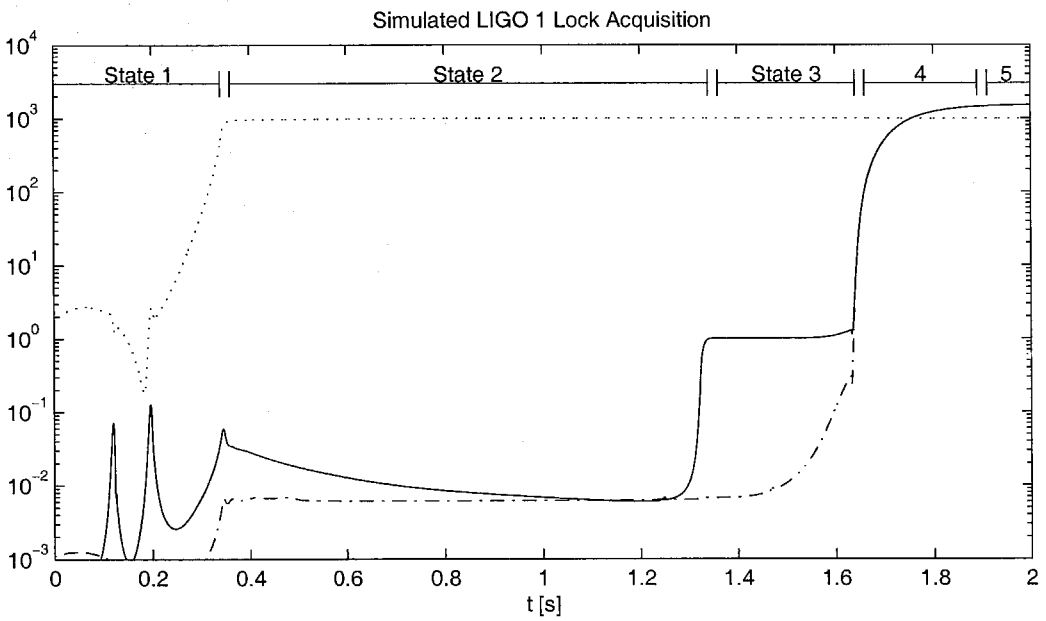

Figure 4.2: A simulated lock acquisition event for a power-recycled interferometer. The state progression is noted at the top of the figure. The time series shown are $\left|A_{POB_1}\right|^2$ (dotted), P_{TRT} (solid), and P_{TRR} (dash-dot.)

4.4 Frequency Response

The topic of frequency response, though critical to the design of a control system, has, for simplicity, not been mentioned in the preceding discussion. The objective of applying the input matrix is to maintain stability of the control loops. If the frequency response of the interferometer to a given degree of freedom is the same at all ports and is independent of the state of the interferometer, maintaining the gain at any one frequency will suffice to accomplish this objective. If, on the other hand, the frequency response of the interferometer to a given degree of freedom is significantly different at different ports or at different times, the sensing matrix must

be constructed with the properties of the control system in mind.

In the LIGO 1 interferometer there are two examples of complicated frequency response. One of these is in the cArm degree of freedom as state 4 progresses. In state 3 the frequency response of all signals to this degree of freedom is that of the arm cavity

$$S_{demod}(\omega) \propto \frac{1}{1 + i\omega/\omega_c}\Delta_{cArm} \tag{4.22}$$

with $\omega_c \sim 100\,\mathrm{Hz}$, but in state 5 the response is that of the coupled cavity with $\omega_c \sim 1\,\mathrm{Hz}$.[26]

To prevent this change from destabilizing the cArm control loop, the sensing matrix must be designed to reflect the change that occurs at the unity gain frequency of the loop, ω_{cArm}. Fortunately, the unity gain frequency for this loop is typically close to the arm cavity pole ($100\,\mathrm{Hz} \lesssim \omega_{cArm} \lesssim 200\,\mathrm{Hz}$) so the transition to the coupled cavity response has no significant effect on the stability of the control loop.

The second example of non-trivial frequency response is found in the signals used to control the PRC degree of freedom. In this case, the frequency response in the two most sensitive signals (I_{REF} and I_{POB}) are similar, and essentially flat, until state 4. During state 4 the frequency responses of these signals change, and in state 5 can be somewhat different from each other,

$$I_{REF}(\omega) \propto \frac{1 + i\omega/\omega_r}{1 + i\omega/\omega_c}\Delta_{PRC} \tag{4.23}$$

$$I_{POB}(\omega) \propto \frac{1 + i\omega/\omega_p}{1 + i\omega/\omega_c}\Delta_{PRC} \tag{4.24}$$

where $\omega_c \sim 1\,\mathrm{Hz}$ is again the coupled cavity frequency, $\omega_r \lesssim 2\,\mathrm{Hz}$ and $\omega_p \sim 0.5\,\mathrm{Hz}$. However, it is again true that the response at the unity gain frequency of the control loop ($\omega_{PRC} \sim 40\,\mathrm{Hz}$) does not change appreciably.[26] Care must be taken, however, to evaluate the elements of the sensing matrix at the unity gain frequency of the control loop rather than at DC since, as in this case, the results may differ significantly.

The general rule applied in these two examples is: If the phase response to a given degree of freedom at the unity gain frequency of the corresponding control loop is

similar at all ports, it is sufficient for the sensing matrix elements to be proportional to the sensing gain at the unity gain frequency. To handle the more general problem of arbitrary frequency dependence a frequency dependent sensing matrix may be used, but the particulars of the LIGO 1 configuration make this level of complexity unnecessary.

Chapter 5

Experiment

This chapter describes the application of the theory and techniques discussed in the previous chapter to the LIGO 1 interferometers.

5.1 Experimental Setup

The apparatus consists of two conceptually separate pieces: the analog and optical hardware, and the digital control software. The analog-to-digital and digital-to-analog converters (ADCs and DACs) represent the interfaces between these pieces. These system components are described separately in the following sections.

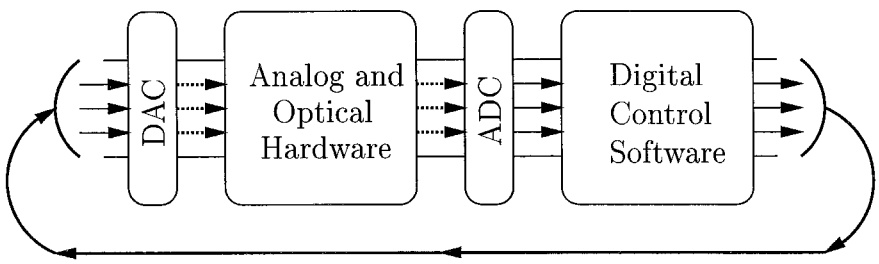

Figure 5.1: Experimental apparatus conceptual pieces.

5.1.1 The Analog and Optical Hardware

There are three LIGO 1 interferometers, two located in the desert at Hanford, Washington, and one in the forest near Livingston, Louisiana. The configuration of the primary interferometer at each site, known as the "4k" interferometer, is shown in figure 4.1. The vast majority of the experimental work was performed from October 2000 to February 2001 with the secondary (a.k.a. "2k") interferometer at the LIGO Hanford Observatory. This interferometer includes two folding mirrors which allow

it to share its vacuum envelope with the 4k interferometer (see figure 5.2), and has somewhat different optical path lengths than the 4k interferometers. Approximate optical parameters for both the 4k and 2k interferometers are given in table 5.1.

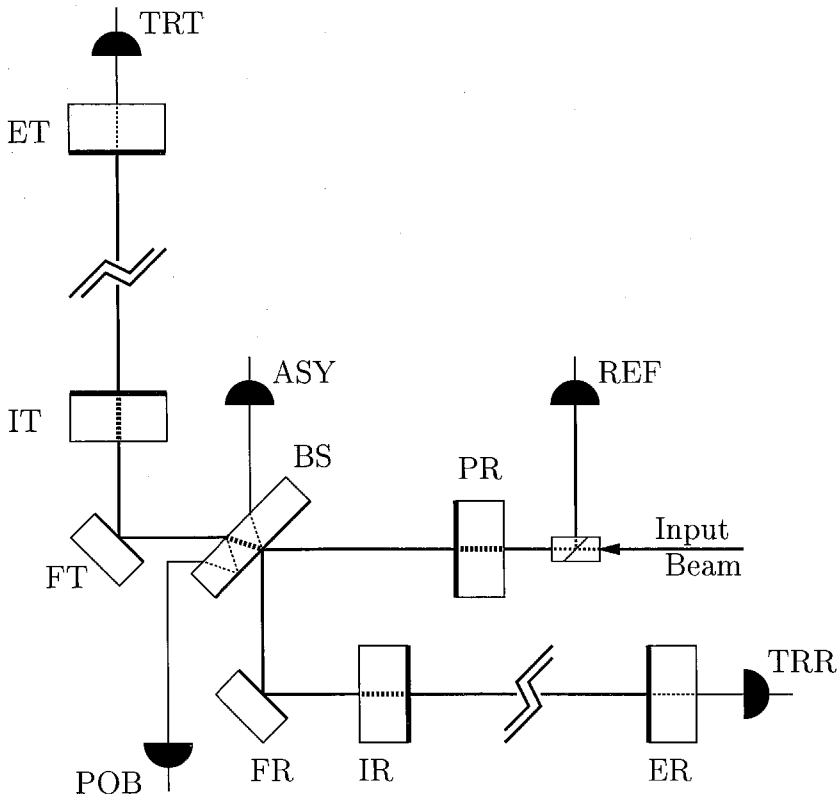

Figure 5.2: LIGO Hanford 2 km optical layout.

The input beam arrives at the PR mirror after being phase modulated ($\Gamma_{mod} = 0.44$) and passing through a mode-cleaner.[27] The input power was variable, most of the experiment was performed with 100 mW incident on PR, but the power was later increased to 1 W.

In addition to the five demod signals that appear in equation (4.6), the LIGO 1 lock acquisition system uses four low frequency (bandwidth $\ll \omega_{mod}$) power signals (P_{REF}, P_{POB}, P_{TRT}, and P_{TRR}), and a signal produced by demodulating at POB at twice the modulation frequency. (Note that this demod signal, known as S_{POB}, is used to measure the sideband power in the recycling cavity and should not be confused with other demod signals, generically know as S_{demod}, which are used to

Optic	t^2	$1 - t^2 - r^2$
PR	2.8%	1000ppm
BS	51%	???
IT and IR	2.8%	70ppm
ET and ER	5ppm	70ppm
FT and FR	5ppm	70ppm

	Primary "4k"	Secondary "2k"
$L_{PR:BS}$	4397 mm	3022 mm
$L_{BS:IT}$	4937 mm	9528 mm
$L_{BS:IR}$	4637 mm	9828 mm
$L_{IT:ET}$ and $L_{IR:ER}$	3995 m	2009 m
$f_{mod} = \omega_{mod}/2\pi$	33.3 MHz	29.5 MHz

Table 5.1: LIGO 1 optical parameters.

produce error signals.) Each of these signals is digitized and made available to the digital control system for real-time processing.

All of the optics in the LIGO 1 interferometers are suspended to provide seismic isolation above the pendulum resonance frequency at 0.74 Hz. The actuators are coil/permanent magnet pairs which produce a force on the optic proportional to the actuation signal produced by the control system, up to a limit of about 10 mN. The mass of each optic is approximately 10.3 kg.

5.1.2 The Digital Control System

The digital control system used in the LIGO 1 interferometers runs on VMIVME 7697 modules, the core of which is a 1GHz Pentium processor. There are three such modules for each interferometer, one at the vertex and one at each end. These modules communicate over an optical reflective memory link. The connection from the digital system to the world of analog electronics is provided by Pentek 6102 ADC/DACs operating at 16384 Hz.

Processing of $\vec{S}_{demod}$ by the digital control system to produce actuation signals for each optic is done in four steps:

1. Compute the input matrix $\mathbf{G}$ (see section 5.3).
2. Multiply the demod signals by the input matrix to produce error signals for each degree of freedom (i.e., $\vec{S}_{err} = \mathbf{G}\vec{S}_{demod}$).
3. Filter the error signals to produce actuation signals for each degree of freedom (see table 5.2 for filter parameters).
4. Multiply the degree of freedom actuation signals by the output matrix, described below, to produce actuation signals for each optic.

Implementation of the first step is discussed in detail in the following sections. Step 2 is simple matrix multiplication, the filters used in step 3 are shown in table 5.2, and a typical output matrix equation for step 4 is

$$\begin{bmatrix} F_{PR} \\ F_{BS} \\ F_{FT} \\ F_{FR} \\ F_{IT} \\ F_{IR} \\ F_{ET} \\ F_{ER} \end{bmatrix} = \begin{bmatrix} 0 & 0 & 0 & 0 \\ 0 & 0 & 0 & 0 \\ 0 & 0 & -\sqrt{2} & -\sqrt{2} \\ 0 & 0 & -\sqrt{2} & \sqrt{2} \\ 0 & 0 & 0 & 0 \\ 0 & 0 & 0 & 0 \\ -1 & -1 & 0 & 0 \\ -1 & 1 & 0 & 0 \end{bmatrix} \begin{bmatrix} F_{cArm} \\ F_{dArm} \\ F_{PRC} \\ F_{Mich} \end{bmatrix}. \tag{5.1}$$

Filter	Purpose	Properties
1	roll-off	Butterworths at 1 kHz and 2 kHz
2	pendulum compensation	zero at 10 Hz
3	cavity pole compensation	zero at 100 Hz
4	low-frequency boost	pole at 0.1 Hz and zero at 10 Hz

Degree of Freedom	Filters	Unity Gain Frequency
cArm and dArm	1, 2, 3 and 4 (switchable)	100 to 200 Hz
PRC and Mich	1 and 2	30 to 50 Hz

Table 5.2: LIGO 1 digital filter bank.

5.1.3 Sources of Excitation

There are two primary sources of excitation against which the interferometer control systems must work: seismic noise and laser frequency noise. Each optic in the interferometer is suspended, and the suspension point is supported by a seismic isolation system which isolates it from the motion of the ground. The motion of the optics due to ground motion, known as seismic noise, varies considerably from day to day and is much larger in Livingston than in Hanford, but a representative spectrum of suspension point motion along the optic axis is shown in figure 5.3.

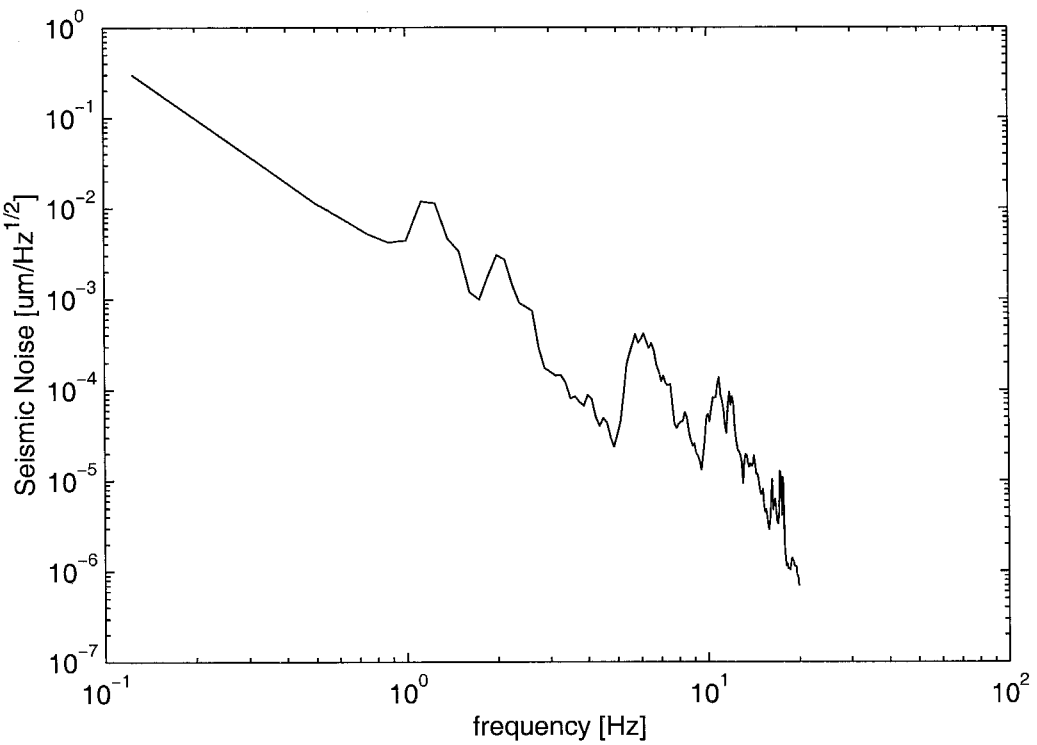

Figure 5.3: Seismic motion is one of the primary sources of excitation that a lock acquisition system must contend with. The amount of seismic motion varies greatly with location, time of day, weather, and other factors. These data were taken with the Hanford 2k interferometer, using the noise in the dArm degree of freedom as a measure of seismic noise in the frequency range shown.

The second source of excitation, frequency noise, is indistinguishable from common mode mirror motion. The equivalent mirror motion, ΔL, for a given change in frequency, Δf, is given by the familiar relationship $\Delta f/f = \Delta L/L$, where f and

L are the initial frequency and length. The frequency noise spectrum of the light incident on the PR is shown in figure 5.4.

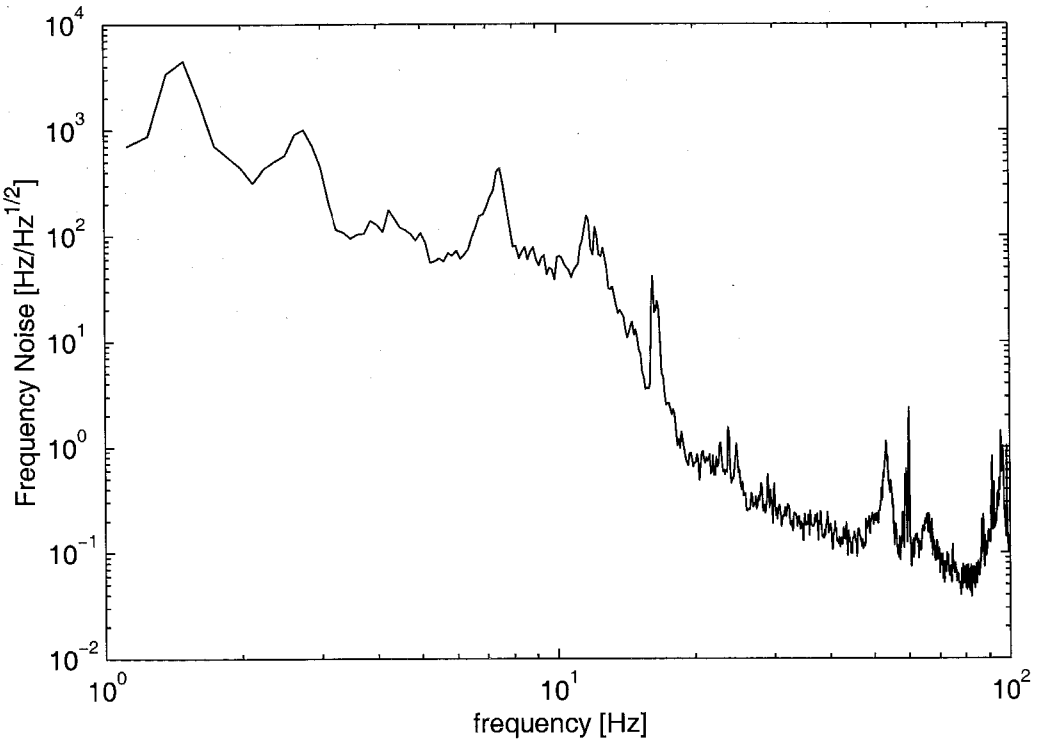

Figure 5.4: Frequency noise on the input beam is equivalent to common mode motion of the optics. At the time this data was taken, frequency noise dominated over seismic noise above 1 Hz for the Hanford 2k interferometer arms. The frequency-to-length conversion factor, in this case, is $7.1 \times 10^{-6}\,\mu\mathrm{m}/\sqrt{\mathrm{Hz}}$.

5.2 Detection Mode Control Scheme

Control of the interferometer is relatively simple in the operational state, known as "Detection Mode," and the input matrix for this state is the same as that used by the lock acquisition system in state 5, except that $A_{\_} = 0$ is asserted for simplicity

(see section 4.3.5). In this state the input matrix equation is

$$\begin{bmatrix} S_{err_{PRC}} \\ S_{err_{cArm}} \\ S_{err_{dArm}} \end{bmatrix} = \begin{bmatrix} G^{DM}_{PRC,I_{ref}} & G^{DM}_{cArm,I_{ref}} & 0 & 0 \\ G^{DM}_{PRC,I_{pob}} & G^{DM}_{cArm,I_{pob}} & 0 & 0 \\ 0 & 0 & G^{DM}_{dArm,Q_{asy}} & 0 \\ 0 & 0 & 0 & G^{DM}_{Mich,Q_{pob}} \end{bmatrix}^{-1} \begin{bmatrix} I_{ref} \\ I_{pob} \\ Q_{asy} \\ Q_{pob} \end{bmatrix}, \tag{5.2}$$

where each G^{DM} is the detection mode gain constant for each degree of freedom. This control scheme is discussed in detail in [26].

5.3 Sensing Matrix Estimation

5.3.1 Field Amplitude Estimators

The sensing matrix is determined by the amplitudes of three resonant fields ($A_{\pm}$ and A_{PRM}), and six local oscillator fields (A_{ASY_1}, A_{POB_0}, A_{POB_1}, A_{REF_0}, A_{REF_1}, and A_{REF_2}; see section 4.1.2). Each of these must be inferred from measurement, the more directly the better.

According to equation (4.17), $\left|A^{fo}_{IT_0}\right|^2$, $\left|A^{fo}_{IR_0}\right|^2$ and $A^{fo}_{PR_0}$ are all necessary to estimate $A_{\pm}$. Measurements of the power transmitted through the arms cavities suffice as estimators of $\left|A^{fo}_{IT_0}\right|^2$ and $\left|A^{fo}_{IR_0}\right|^2$

$$t^2_{ET}\left|A^{fo}_{IT_0}\right|^2 \simeq P_{TRT} \tag{5.3}$$

$$t^2_{ET}\left|A^{fo}_{IR_0}\right|^2 \simeq P_{TRR}. \tag{5.4}$$

The primary assumption here is that contributions to the transmitted power from field components other than the carrier ($j = 0$) are negligible. This assumption is valid along the acquisition path, since the carrier field resonates in the arm cavities in states 3, 4 and 5, and at no point on the path do the sidebands resonate in the arm cavities. Another way to say this is that a sideband resonating in an arm cavity represents a departure from the acquisition path, and thus it also represents a departure from the

region in which these equations are valid and utilized.

Assuming that the fields in the recycling cavity are changing adiabatically and the carrier is well mode-matched into the recycling cavity, $A^{fo}_{PR_0}$ can be estimated by

$$A^{fo}_{PR_0} \simeq \frac{t_{PR}}{1 - r_{Mich_0} r_{PR}} A^{bi}_{PR_0}, \tag{5.5}$$

where $r_{Mich} = A^{fi}_{PR}/A^{fo}_{PR}$ is the amplitude reflectivity of the Michelson and arm cavities treated as a whole. When neither arm cavity is resonant (state 2) the recycling cavity is anti-resonant for the carrier. In this state the carrier light interferes destructively at the ASY port and $r_{Mich_0} \simeq -1$, which implies that

$$A^{fo}_{PR_0} \simeq \frac{t_{PR}}{1 + r_{PR}} A^{bi}_{PR_0}. \tag{5.6}$$

When only one arm cavity is resonant (state 3) the change in sign of the over-coupled cavity causes the carrier light to interfere constructively at the ASY port, making $r_{Mich_0} \simeq 0$ and

$$A^{fo}_{PR_0} \simeq t_{PR}\, A^{bi}_{PR_0}. \tag{5.7}$$

When both arm cavities are resonant (states 4 and 5), r_{Mich_0} is less than one by a small and variable amount. A robust estimator for $A^{fo}_{PR_0}$ in these states can be derived from the arm cavity amplitudes. Since

$$A^{fo}_{IT_0} = \frac{\alpha_{T_0}}{\sqrt{2}} \frac{t_{IT}}{1 - r_{IT} r_{ET}} A^{fo}_{PR_0} \tag{5.8}$$

$$A^{fo}_{IR_0} = \frac{\alpha_{R_0}}{\sqrt{2}} \frac{t_{IR}}{1 - r_{IR} r_{ER}} A^{fo}_{PR_0}, \tag{5.9}$$

where $0 < \{\alpha_{T_0}, \alpha_{R_0}\} < 1$ are the mode-matching coefficients[1] for the arm cavities.

[1] These "mode-matching coefficients" were not included in the theory discussions of chapters 3 and 4, but are needed experimentally to quantify the imperfect spatial overlap of a cavity's eigenmode with the input field. Quantitatively, α is the overlap integral of the cavity eigenmode with the input field, typically $0.5 < \alpha \lesssim 1$.

Inverting this equation yields

$$A^{fo}_{PR_0} \simeq \sqrt{2}\,\frac{1 - r_{IT}r_{ET}}{t_{IT}}\,\max\left(A^{fo}_{IT_0}, A^{fo}_{IR_0}\right), \tag{5.10}$$

assuming that at least one of $\{\alpha_{T_0}, \alpha_{R_0}\} \sim 1$.

These estimators are combined to produce $A_{\pm}$ as follows: in state 2, when neither arm is near resonance,

$$A_{\pm} \simeq 0 \tag{5.11}$$

in state 3

$$A_{\pm} \simeq t_{PR}t^2_{ET}\,\frac{P_{TRT} \pm P_{TRR}}{A^{bi}_{PR_0}}, \tag{5.12}$$

and in states 4 and 5

$$A_{\pm} \simeq \frac{t_{IT}t_{ET}}{1 - r_{IT}r_{ET}}\,\frac{P_{TRT} \pm P_{TRR}}{\sqrt{2\max(P_{TRT}, P_{TRR})}}. \tag{5.13}$$

Since the input power and modulation depth are directly measurable and relatively constant, $A^{bi}_{PR_j}$ is easily determined. One of the pick-off local oscillator fields, A_{POB_0}, is also available from these measurements since it is simply proportional to $A^{fo}_{PR_0}$,

$$A_{POB_0} = t_{POB}A^{fo}_{PR_0} \tag{5.14}$$

where t_{POB} is the amplitude "transmissivity" of the optical train leading from the PR to the POB detector.

A_{PRM} is estimated with the aid of a signal produced by demodulation of the field at POB at twice the modulation frequency,

$$S_{POB} \simeq -t^2_{POB}\,\mathcal{R}e\left(A^{fo\star}_{PR_{-1}}A^{fo}_{PR_1} + A^{fo\star}_{PR_{-2}}A^{fo}_{PR_0} + A^{fo\star}_{PR_0}A^{fo}_{PR_2}\right) \tag{5.15}$$

$$\simeq t^2_{POB}\left[\left|A^{fo}_{PR_1}\right|^2 - 2\left|A^{fo}_{PR_0}A^{fo\star}_{PR_2}\right|\right]. \tag{5.16}$$

This signal is a valid estimator for

$$A^{fo}_{PR_1} \simeq \frac{\sqrt{S_{POB}}}{t_{POB}} \tag{5.17}$$

when $\left|A^{fo}_{PR_0} A^{fo\star}_{PR_2}\right| \ll \left|A^{fo}_{PR_1}\right|^2$, a condition that is satisfied at all points on the acquisition path after the acquisition of state 2 since the second-order sidebands are anti-resonant in the recycling cavity throughout. The estimator used for A_{PRM}, a slight modification of equation (4.18) which allows for imperfect optics, is

$$A_{PRM} \simeq \frac{\left|A^{fo}_{PR_1}\right|^2}{\alpha_{PRM_1} A^{bi}_{PR_1}}, \tag{5.18}$$

where α_{PRM_1} is the mode-matching coefficient for the first-order sidebands into the recycling cavity. Unfortunately, no independent measure of α_{PRM} is available, so one must either assume that the cavity's alignment is sufficiently stable to treat α_{PRM} as a constant, or that the cavity is exactly resonant such that

$$\alpha_{PRM_1} = \frac{1 - r_{Mich_1} r_{PR}}{t_{PR}} \frac{A^{fo}_{PR_1}}{A^{bi}_{PR_1}}. \tag{5.19}$$

Since the particulars of the interferometer make the latter assumption more plausible, our estimator is

$$A_{PRM} \simeq \frac{t_{PR}}{1 - r_{Mich_1} r_{PR}} \frac{\sqrt{S_{POB}}}{t_{POB}}, \tag{5.20}$$

where $r_{Mich_1} \simeq \sqrt{1 - t^2_{Mich_1}}$ and $t^2_{Mich_1}$ is assumed to be dominated by the transmission of sidebands to the ASY port provided by the Schnupp asymmetry,

$$t_{Mich_1} \simeq \sin\left(2\pi \frac{\omega_{mod}\left[L_{BS:IT} - L_{BS:IR}\right]}{2\pi c}\right). \tag{5.21}$$

S_{POB} is also used directly in estimates of the local oscillator field amplitudes A_{POB_1} and A_{ASY_1}. A_{POB_1} is estimated by

$$A_{POB_1} \simeq \sqrt{S_{POB}}, \tag{5.22}$$

and, similarly,

$$A_{ASY_1} \simeq t_{Mich_1} \frac{\sqrt{S_{POB}}}{t_{POB}}. \tag{5.23}$$

This leaves the three reflected fields. The second-order sideband field, which does not resonate in the interferometer at any point on the acquisition path, can be estimated directly from the input field

$$A_{REF_2} \simeq A^{bi}_{PR_2}. \tag{5.24}$$

Since the first-order sidebands resonate in the recycling cavity, but are poorly mode-matched in the "cold" LIGO 1 interferometers,[2] the reflected field is estimated in two parts: mode-matched (A_{REFm_1}), and non-mode-matched (A_{REFn_1}). The estimators for these two components are

$$A_{REFm_1} = r_{PR}\,\alpha_{PRM_1}\,A^{bi}_{PR_1} - t_{PR}\,r_{Mich_1}\,A^{fo}_{PR_1} \tag{5.25}$$

$$A_{REFn_1} = r_{PR}\sqrt{1-\alpha^2_{PRM_1}}A^{bi}_{PR_1} \tag{5.26}$$

where equations (5.17) and (5.19) are used to estimate $A^{fo}_{PR_1}$ and α_{PRM_1}. Each of these components will have some overlap with the interferometer's carrier eignemode and will contribute to the demodulated signal. The effective local oscillator is taken to be a linear combination of the components

$$A_{REF_1} \simeq \alpha_{REFm} A_{REFm_1} + \alpha_{REFn} A_{REFn_1}. \tag{5.27}$$

Measurement of these mode overlap coefficients remains a technical challenge, but $\alpha_{REFm} = 1$ and $\alpha_{REFn} = 1$ is sufficiently accurate to allow for lock acquisition.

The reflected carrier amplitude can be computed in a similar fashion, with the

[2]The LIGO 1 optics are designed to be well mode-matched in the presence of thermal lensing. Lock acquisition, however, must take place before the optics can be heated by the resonant fields.

simplification that it is assumed to be well mode-matched,[3]

$$A_{REF_0} = r_{PR}\, A^{bi}_{PR_0} - t_{PR}\, r_{Mich_0}\, A^{fo}_{PR_0}, \tag{5.28}$$

where r_{Mich_0} and $A^{fo}_{PR_0}$ are as discussed above (see equations (5.5) through (5.10)), except that in this context $r_{Mich_0} \simeq 1$ will suffice in states 4 and 5. This estimate is, however, further complicated by the existence of the reflected power measurement, P_{REF}, which should satisfy

$$P_{REF} = \left|A_{REF_0}\right|^2 + \left|A_{REFm_1}\right|^2 + \left|A_{REFn_1}\right|^2 + \left|A_{REF_2}\right|^2. \tag{5.29}$$

Since P_{REF} is typically dominated by $\left|A_{REF_0}\right|^2$, it seems plausible that equation (5.29) can be used to produce a more robust measure of $\left|A_{REF_0}\right|^2$ than estimation via equation (5.28). This strategy is, in fact, the one used in the LIGO 1 lock acquisition system, with the sign ambiguity resolved by taking the sign of A_{REF_0} given by equation (5.28).

5.3.2 Calibration of Power Signals

Three power measurements (P_{TRT}, P_{TRR} and P_{REF}) and one demodulated signal (S_{POB}) are used in the field amplitude estimators described in the previous section. Since S_{POB} is difficult to calibrate directly, the power measurement at the same port, P_{POB}, is also needed. The unitless calibrated measurements, represented by an overbar, are relative to the input power,

$$P_{IN} \equiv \sum_j A^{bi}_{PR_j}. \tag{5.30}$$

P_{REF} and P_{POB} are calibrated with IT and IR misaligned and PR aligned. In this

[3]Since the carrier resonates in the arm cavities it is not sensitive to the nearly degenerate nature of the power recycling cavity. This feature insures that, unlike the sidebands, the carrier is always well mode-matched (i.e., $\alpha_{PRM_0} \sim 1$)..

configuration[4]

$$\bar{P}_{REF} \equiv \frac{P_{REF}}{P_{IN}} = r_{PR}^2 \tag{5.31}$$

and

$$\bar{P}_{POB} \equiv \frac{P_{POB}}{t_{PR}^2 P_{IN}} = 1. \tag{5.32}$$

The transmitted arm power calibration is performed by misaligning IR and PR, then locking the aligned arm cavity. If the mean alignment is good

$$\bar{P}_{TRT} \equiv \left[\frac{\sqrt{2}}{\alpha_{T_0}} \frac{1 - r_{IT} r_{ET}}{t_{IT} t_{ET}}\right]^2 \frac{P_{TRT}}{J_0(\Gamma_{mod})^2 t_{PR}^2 P_{IN}} \simeq 1 \tag{5.33}$$

when the power is at its highest points (i.e., $\alpha_{T_0}^2 \sim 1$). A symmetric configuration is used to calibrate P_{TRR}.

To calibrate S_{POB}, ET and ER were misaligned and the recycling cavity locked (state 2). It is important to note that, like locking a simple Fabry-Perot cavity, this can be achieved without a sophisticated lock acquisition system (i.e., just enabling the control loops suffices). In this state

$$\bar{S}_{POB} \equiv \frac{S_{POB}}{J_1(\Gamma_{mod})^2 t_{PR}^2 P_{IN}} \simeq \frac{\bar{P}_{POB}}{2\, J_1(\Gamma_{mod})^2}. \tag{5.34}$$

5.3.3 Gain Coefficients

The last set of ingredients necessary to estimate the sensing matrix are the gain coefficients that appear in equations (4.7) through (4.16). Unlike field amplitudes, which can change rapidly, the gain coefficients need only be measured when the interferometer response they quantify changes (e.g., the interferometer's mean alignment is changed, the sensing electronics are changed, etc.).

The general procedure for measuring a gain coefficient is as follows:

[4] At the time of this experiment, the signal for P_{POB} was actually taken from P_{POT} (see figure 1.4). Calibration was performed with all the mirrors except IT misaligned such that $P_{POB} = P_{POT}$.

1. Put the interferometer in a state in which the gain coefficient to be measured appears in a non-zero element of $\mathbf{M}$, call it $\mathbf{M}_{p,q}$.
2. Measure the transfer of an excitation in $\vec{\Delta}_q$ to $\vec{S}_{err_p}$ (typically near the unity gain frequency of the loop controlling $\vec{\Delta}_q$).
3. Multiply the gain coefficient by the measured transfer amplitude.

It is often beneficial to repeat this procedure until the gain coefficient converges on some stable value.

Note that this procedure requires the interferometer to be locked in a particular state, which can be problematic if the gain coefficient to be measured is required to reach that state. The LIGO 1 lock acquisition system is designed to avoid this "chicken-and-egg" problem by bootstrapping off easily acquired states. The complete gain coefficient measurement procedure is

1. As in the measurement of S_{POB}, lock state 2 and measure g_{Pref}, g_{Ppob}, g_{Mref}, and g_{Mpob}.
2. As in the measurement of P_{TRT} or P_{TRR}, lock either arm cavity using I_{asy}. Replace Q_{asy} with I_{asy} in $\vec{S}_{demod}$ and measure g_{Aasy}. This replacement is necessary to compensate for the absence of the Michelson which, when present, rotates the local oscillators for this signal (A_{ASY_1} and $A_{ASY_{-1}}$) by $\pi/2$.
3. Lock the recycling cavity and the transmitted arm (state 3) with ER misaligned and measure all of the gain coefficients. For the previously measured coefficients, the results should be similar.
4. Switch to the reflected arm and remeasure all of the gain coefficients. The results should be similar to those measured in step 3.

5.4 Implementation

This section discusses the implementation details of the lock acquisition algorithm used in the LIGO 1 interferometers. The algorithm performs two types of actions: continuous changes in $\mathbf{G}$ which compensate for continuous changes in $\tilde{\mathbf{M}}$, and discon-

tinuous changes in $\mathbf{G}$ which result from changes in the size of $\tilde{\mathbf{M}}$. The discontinuous changes occur at the state boundaries discussed in section 4.3 and on either side of the DS singularity that is crossed in state 4. Each of these discontinuous changes is marked in the algorithm by a state bit and recognized via a trigger of some sort.

5.4.1 Discontinuous Changes: Triggers and Bits

The state progression begins with the departure from state 1. As the recycling cavity becomes resonant, S_{POB} increases and it remains at an elevated level all along the acquisition path. Furthermore, carrier resonances in the recycling cavity produce a negative signal (see equation (5.15)), a fact that makes S_{POB} a particularly good indicator of state 2 since spurious carrier resonances are easily rejected. For these reasons, the trigger which recognizes the transition from state 1 to state 2 and beyond is based on the value of S_{POB}. This trigger has distinct on and off levels to prevent noise from toggling the state. These levels are called "RecOn" and "RecOff" and the associated bit is "Engaged." To reiterate, the Engaged bit is set when $S_{POB} > T_{RecOn}$ and is reset when $S_{POB} < T_{RecOff}$.

State 3 is entered when one of the two arms becomes resonant for the carrier. The power buildup in the cavities, as measured by the transmitted power signals, $\bar{P}_{TR\{T,R\}}$, is used to recognized the approach of resonance ($\bar{P}_{TR\{T,R\}} > T_{ArmOn}$) and the passage of resonance ($\bar{P}_{TR\{T,R\}} < T_{ArmOff}$). The corresponding state bits are labeled "ArmTOn" and "ArmROn." When one of these bits is set, along with the Engaged bit, the interferometer is in state 3.

Entry into state 4 is indicated when both arm bits and the Engaged bit are set. The passage of the DS singularity in state 4 is marked by the "InvBad" bit. This bit is set anytime the absolute value of the normalized determinant of $\mathbf{M}$ is less than the threshold value "DetNormMin."

Also in the course of state 4 the Δ_{Mich} degree of freedom transitions from Q_{ref} to Q_{pob} to avoid a zero in the reflected signal gain. This transition is accomplished by simply switching signals at a predetermined arm power level dubbed "MichSwitch."

5.4.2 Continuous Changes: The Input Matrix in Each State

State 1: Not Engaged

In this state **M** is essentially unknown so there is little to be done but wait for state 2 to happen by chance. At the Hanford site some excitation is necessary and is provided by setting

$$\mathbf{G}_{I_{ref},PRC} = c_{push}/g_{Pref} \tag{5.35}$$

and

$$\mathbf{G}_{Q_{ref},Mich} = c_{push}/g_{Mref} \tag{5.36}$$

where c_{push} is an adjustable parameter.

State 2: Engaged

In state 2 Δ_{Mich} and Δ_{PRC} are controlled. Δ_{Mich}, being rather separate in **M** is dealt with separately. Until state 4 the error signal for Δ_{Mich} is produced entirely from Q_{ref} via

$$\mathbf{G}_{Q_{ref},Mich} = G^{-1}_{Mich,Q_{ref}}. \tag{5.37}$$

In this state the error signal for PRC comes from I_{ref} via

$$\mathbf{G}_{I_{ref},PRC} = G^{-1}_{PRC,I_{ref}} \tag{5.38}$$

and the error signals for cArm and dArm are zero.

State 3: Engaged and one Arm Locked

As a NS singularity is removed from **M**, a 2x2 matrix inversion is performed to produce error signals for Δ_{PRC} and Δ_{cArm}

$$\begin{bmatrix} S_{err_{PRC}} \\ S_{err_{cArm}} \end{bmatrix} = \begin{bmatrix} G_{PRC,I_{ref}} & G_{cArm,I_{ref}} \\ 0 & G_{cArm,Q_{asy}} \end{bmatrix}^{-1} \begin{bmatrix} I_{ref} \\ Q_{asy} \end{bmatrix} \tag{5.39}$$

and $S_{err_{dArm}} = \pm S_{err_{cArm}}$ depending on which arm is resonant.

States 4 and 5: Engaged and both Arms Locked

As state 4 is entered and the last NS singularity is removed from **M** and the input matrix expands again to

$$\begin{bmatrix} S_{err_{PRC}} \\ S_{err_{cArm}} \\ S_{err_{dArm}} \end{bmatrix} = \begin{bmatrix} G_{PRC,I_{ref}} & G_{cArm,I_{ref}} & G_{dArm,I_{ref}} \\ G_{PRC,I_{pob}} & G_{cArm,I_{pob}} & G_{dArm,I_{pob}} \\ 0 & G_{cArm,Q_{asy}} & G_{dArm,Q_{asy}} \end{bmatrix}^{-1} \begin{bmatrix} I_{ref} \\ I_{pob} \\ Q_{asy} \end{bmatrix}. \quad (5.40)$$

As the determinant of the 3x3 matrix shown above becomes small the signals for Δ_{PRC} and Δ_{cArm} become inseparable. This DS singularity forces a choice between controlling Δ_{cArm} or Δ_{PRC}. Since Δ_{cArm} dominates in both I_{ref} and I_{pob}, and since it is far more sensitive to the excitation sources than Δ_{PRC}, the error signal equation is reduced to

$$\begin{bmatrix} S_{err_{cArm}} \\ S_{err_{dArm}} \end{bmatrix} = \begin{bmatrix} G_{cArm,I_{ref}} & G_{dArm,I_{ref}} \\ G_{cArm,Q_{asy}} & G_{dArm,Q_{asy}} \end{bmatrix}^{-1} \begin{bmatrix} I_{ref} \\ Q_{asy} \end{bmatrix}, \quad (5.41)$$

and $S_{err_{PRC}} = 0$ until the DS singularity passes. Assuming the power in the interferometer continues to grow, the absolute value of the normalized determinant of the matrix in equation (5.40) will exceed DetNormMin and control of all degrees of freedom will be reestablished.

Finally, when $\bar{P}_{TR\{T,R\}}$ increases beyond $T_{MichSwitch}$, Δ_{Mich} is switched to Q_{pob} by setting $M_{Q_{ref},Mich} = 0$ and

$$\mathbf{G}_{Q_{pob},Mich} = G^{-1}_{Mich,Q_{pob}}. \quad (5.42)$$

5.5 Experimental Results

At the time of this writing only the Hanford 2k interferometer has been locked stably in its final configuration. This interferometer has been locked repeatedly (over one hundred times) and, if left undisturbed, will typically hold lock until the available actuators run out of range due to tidal stretching of the Earth's surface. After each loss of lock event the interferometer requires about a minute to damp the excited optics and, when well aligned, will reacquire lock in less than twenty minutes. The mean-time-to-lock demonstrated in this experiment varies considerably depending on the state of the interferometer and its environment, but is consistently short enough to have no significant impact on the duty-cycle of the detector, which is expected to hold lock for days, if not weeks, at a time once all of the actuators and controllers are functioning.

In addition to the indirect evidence provided by a locking interferometer, the correctness of the input matrix computed for lock acquisition was tested directly by measurement of the gain coefficients in state 3 and state 5. If the sensing matrix equations are correct, these coefficients should have the same value in all states, but since the full interferometer cannot be locked without them, they must initially be measured with the interferometer in state 3. When remeasured in state 5, the values of all gain coefficients were found to agree with the state 3 measurements within measurement error, which was typically less than 20%.

A lock acquisition time series for the Hanford 2k interferometer is shown in figure 5.5. Comparing this event with the last second of the simulated event shown in figure 4.2 reveals considerable similarity, though no arrangement was made to ensure this. Two immediate differences are that the arms locked in the opposite order, and that P_{TRT} in the experimental data shows 3 resonance approaches that did not lock while the simulated event shows no such events after acquisition of state 2. These differences are inevitable, given the random nature of such events, but consistent differences are also present. Systematically lower power levels in the physical interferometer result from imperfect mode-matching, particularly for the sidebands in the recycling cavity

(as seen in S_{POB}), and from imperfect alignment, which degrades the carrier buildup (as seen in P_{TRT} and P_{TRR}) by allowing power to escape through the ASY port.

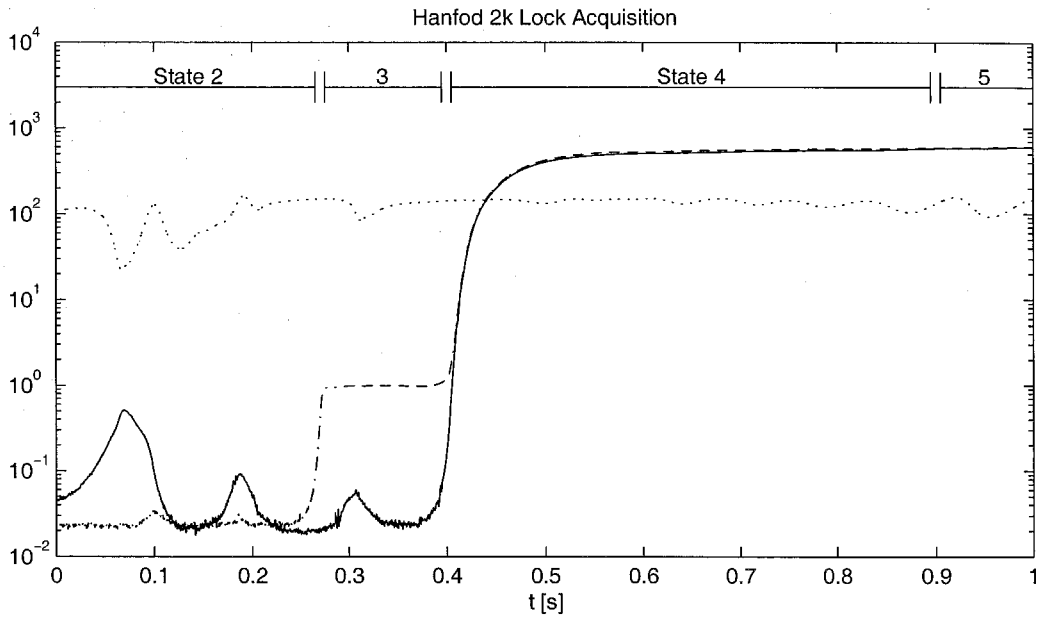

Figure 5.5: A lock acquisition event at the Hanford 2k power-recycled interferometer. Similar to the simulated acquisition event shown in figure 4.2, the state progression is noted at the top of the figure and the time series shown are S_{POB} (dotted), P_{TRT} (solid), and P_{TRR} (dash-dot).

Chapter 6

Conclusion

A considerable amount of time is spent designing a detector for good sensitivity in the operating state, but care must also be taken to ensure that the detector will be able to reach that state. This is not a statement about the gradual process of increasing a detector's sensitivity by removing noise sources, but rather about the swift and dynamic process of lock acquisition. Since lock acquisition may demand greater dynamic range and higher bandwidth of existing signals than the control system used in the operational state of the detector, and may require additional diagnostic signals, it can place considerable demands on the detector's sensing and control system. This work presents a general framework for understanding lock acquisition, and thereby allows it to be treated as an integral part of the detector in the design phase, as opposed to leaving it as a problem to be solved as the detector moves toward operation.

The approach presented in this work begins with the identification (by simulation or intuition) of a path which takes the detector from the uncontrolled state to the operational state. The properties of the detector's outputs along this path, embodied in the sensing matrix, must be determined and parameterized in terms of measureables. Finally, a control system which can compute the inverse of the sensing matrix, apply it to the incoming signals, and make the resulting signals available for feedback is needed to close the control loop.

This formalism was experimentally developed and verified on a km-scale gravitational-wave detector. The LIGO 2km interferometer at Hanford was locked using the techniques developed in this work and, in addition to its demonstrative role, the success of the experiment was a critical step in making the initial LIGO detectors operational.

It is hoped, and expected, that this work will be applicable to both the generation of detectors currently under construction around the world, and to future detector configurations. Applied in the design phase, a firm understanding of lock acquisition

will allow for sophisticated interferometers to be constructed with confidence in their operability.

Appendix A

The Fabry-Perot Cavity

A.1 Cavity Statics

Under the assumptions of perfect alignment and mode-matching, the Fabry-Perot cavity has only one degree of freedom: the round-trip phase $\phi(t)$. This degree of freedom can be completely accounted for by its effect on the intra-cavity electric field leaving the input mirror at time t, $E_I^{fo}(t)$, which will hence forth be referred to simply as $E(t)$. The iterative equation for $E(t)$ is

$$E(t) = t_I\, E_{IN}(t) + r_I r_E e^{i\,\phi(t-T)}\, E(t-2T)\,, \tag{A.1}$$

where $T = L_{I:E}/c$ is the one-way trip time in the cavity, and $\phi(t)$ is the round-trip phase of the intra-cavity field that left the input mirror at time $t-T$, was reflected off the end mirror at time t, and returned to the input mirror at time $t+T$. It is assumed that mirror displacements are small relative to the cavity length so that T may be held constant.

Considerable simplicity can be gained by measuring the phases of all fields relative to that of $E_{IN}(t)$. The two primary simplifications are that no $e^{i\omega t}$ term is necessary in any of the equations and phase noise on the input field is accounted for by $\phi(t)$. If the amplitude of the input field is assumed to be constant, $E_{IN}(t)$ can be replaced by a real constant, E_{IN}.

For a static, or adiabatically changing $\phi(t)$, equation (A.1) can be solved by taking the limit as $T \to 0$,

$$E(t) = \frac{t_I}{1 - r_I\, r_E\, e^{i\,\phi(t)}} E_{IN}. \tag{A.2}$$

The reflected field is the sum of the promptly reflected input field and the leakage

field from the cavity

$$E_I^{bo}(t) = \left[r_I E_{IN} - t_I\, r_E\, e^{i\,\phi(t)}\, E(t)\right] e^{2ikz_I}. \tag{A.3}$$

A.2 Cavity Dynamics

For high finesse cavities it is common to have resonance crossings that occur at an essentially fixed velocity. These crossings produce a characteristic waveform from which the velocity of the crossing can be determined, along with the finesse of the cavity and the demodulation phase. Though some work has been done on producing an analytic expression for this waveform, simple, continuous form has proven elusive.[28] The follow derivation arrives at two easily computed continuous approximations that are suitable for a variety of applications, including fitting experimental data.

For the special case in which $\phi(t) = 2\beta t$, where β is a constant, equation (A.1) can be rewritten as

$$E(t) = t_I E_{IN} \sum_{n=0}^{\infty} e^{i\alpha n^2 - 2i[\beta t - i\gamma]n} \tag{A.4}$$

where $\gamma \equiv -\ln(r_I r_E)/2 = T/\tau$, $\alpha \equiv 2\beta T$, and τ is the decay time of the cavity. This special case can be realized by fixing the input field frequency and the input mirror while moving the end with constant velocity v_E, in which case $\beta = -kv_E$. Equivalently, one can move the input mirror ($\beta = -kv_I$), sweep the frequency of the input field ($\beta = \frac{dk}{dt}T$), or perform any linear combination of the three.

For high finesse cavities with slowly changing phase ($\gamma \ll 1$ and $\alpha \ll 1$), the sum can be converted to an integral giving

$$E(t) \cong \hat{E}(t) \equiv t_I E_{IN} \int_0^{\infty} e^{i\alpha x^2 - 2i[\beta t - i\gamma]x} dx. \tag{A.5}$$

Completing the square and changing the integration variable results in

$$\hat{E}(t) = t_I E_{IN} e^{-i\eta^2}\, \sqrt{\alpha}\, \mathbb{I}_0 \tag{A.6}$$

where

$$\mathbb{I}_0 \equiv \int_0^\infty e^{i[z-\eta]^2} dz, \tag{A.7}$$

and $\eta \equiv \eta_R + i\eta_I \equiv [\beta t - i\gamma]/\sqrt{\alpha}$.

Extending the integration variable to the complex plane provides some insight into the mathematical problem. The first step is to deform the contour and break it into several pieces (see figure A.1) such that

$$\mathbb{I}_0 = \mathbb{I}_1 + \mathbb{I}_2 + \mathbb{I}_3 + \mathbb{I}_4. \tag{A.8}$$

We will attack each of these pieces in turn, starting with $\mathbb{I}_4$ and working back to $\mathbb{I}_1$.

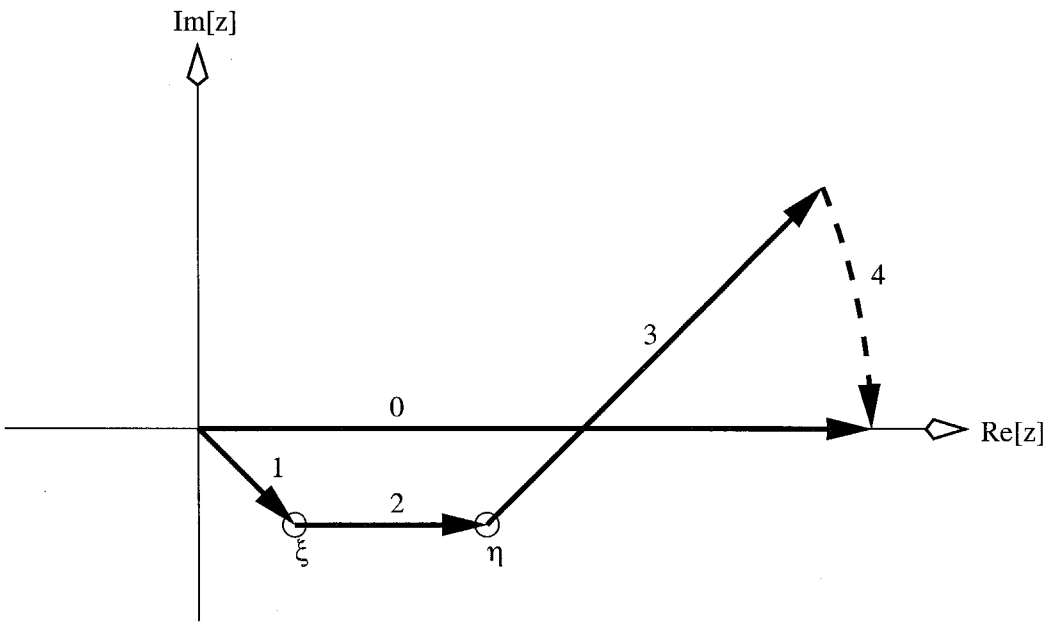

Figure A.1: Deformed contour integral segments. $\xi \equiv [i-1]\,\eta_I$

$\mathbb{I}_4$ closes the contour by connecting $\mathbb{I}_3$ to $\mathbb{I}_0$ at infinity. This integral can be shown to be zero by making the substitution

$$z = r_4 e^{i\phi_4} \tag{A.9}$$

and showing that

$$\lim_{r_4 \to \infty} \sigma_4 \to -\infty \; \forall \; 0 \leq \phi_4 < \pi/4 \tag{A.10}$$

where $\sigma_4 \equiv \mathcal{R}e\Big(i\left[r_4 e^{i\phi_4} - \eta\right]^2\Big)$. Expanding the square and taking the real part leads to

$$\sigma_4 = -r_4^2 \sin(2\phi_4) + 2r_4[\sin(\phi_4)\,\eta_R + \cos(\phi_4)\,\eta_I] + \eta^2. \tag{A.11}$$

The first term ensures that

$$\lim_{r_4 \to \infty} \sigma_4 \to -\infty \; \forall \; 0 < \phi_4 < \pi/4, \tag{A.12}$$

and for $\phi_4 = 0$

$$\sigma_4 = 2r_4 \cos(\phi_4)\,\eta_I + \eta^2, \tag{A.13}$$

which also goes to $-\infty$ since $\eta_I < 0$ for all physical choices of γ and α.

The contour used in $\mathbb{I}_3$ is arrived at by making the substitution [1]

$$z = \sqrt{i}\; z_3 + \eta. \tag{A.14}$$

The resulting integral,

$$\mathbb{I}_3 = \sqrt{i} \int_0^\infty e^{-z_3^2} dz_3, \tag{A.15}$$

evaluates to $\mathbb{I}_3 = \sqrt{i\pi}/2$.

To evaluate $\mathbb{I}_2$ we make the substitution

$$z = -z_2 + \eta, \tag{A.16}$$

which leads to

$$\mathbb{I}_2 = \int_0^{[\eta_R + \eta_I]} e^{iz_2^2} dz_2. \tag{A.17}$$

[1] Throughout this paper $\sqrt{i}$ will be taken to mean $e^{i\pi/4}$.

This integral can be rewritten in terms of the Fresnel integrals as

$$\mathbb{I}_2 = \sqrt{\frac{\pi}{2}}\left[\mathrm{C}\left(\sqrt{\frac{2}{\pi}}[\eta_R+\eta_I]\right)+i\,\mathrm{S}\left(\sqrt{\frac{2}{\pi}}[\eta_R+\eta_I]\right)\right]. \tag{A.18}$$

For $\mathbb{I}_1$ we will resort to approximation. Using the substitution

$$z = \frac{z_1}{\sqrt{i}} \tag{A.19}$$

and expanding the square results in

$$\mathbb{I}_1 = \frac{e^{i\eta^2}}{\sqrt{i}}\int_0^{-\sqrt{2}\ \eta_I} e^{z_1^2+2\sqrt{i}\ \eta z_1}dz_1. \tag{A.20}$$

Replacing the first term in the exponential with its Taylor expansion about $z_1 = 0$ gives

$$\mathbb{I}_1 = \frac{e^{i\eta^2}}{\sqrt{i}}\sum_{n=0}^{\infty}\int_0^{-\sqrt{2}\ \eta_I}\frac{z_1^{2n}}{n!}e^{2\sqrt{i}\ \eta z_1}dz_1. \tag{A.21}$$

Finally, evaluating the integral we obtain

$$\mathbb{I}_1 = \frac{e^{i\eta^2}}{\sqrt{i}}\sum_{n=0}^{\infty}\frac{[2n]!}{n!\left[2\sqrt{i}\ \eta\right]^{2n+1}}\left[1-e^{\sqrt{8i}\ \eta\eta_I}\sum_{m=0}^{2n}\frac{\left[-\sqrt{8i}\ \eta\eta_I\right]^m}{m!}\right]. \tag{A.22}$$

Given that we started with a summation equation (A.4) which seems much simpler than this result, one might wonder what has really been gained. The advantage of this expression is that we may discard all but the first few terms in the outer summation (typically up to $n \simeq 5$). The exact number of terms to keep, which depends on the parameters and the desired accuracy, is best determined empirically.

Since the Fresnel integrals are not as common as the error function, it is worth noting that a slight change in the integration contour (see figure A.2) removes the need for Fresnel integrals. Extending contours 1 and 3 such that $\mathbb{I}_0 = \bar{\mathbb{I}}_1 + \bar{\mathbb{I}}_3$ leads to

$$\bar{\mathbb{I}}_1 = \frac{e^{i\eta^2}}{\sqrt{i}}\sum_{n=0}^{\infty}\frac{[2n]!}{n!\left[2\sqrt{i}\ \eta\right]^{2n+1}}\left[1-e^{-\sqrt{2i}\ \eta[\eta_R-\eta_I]}\sum_{m=0}^{2n}\frac{\left[\sqrt{2i}\ \eta[\eta_R-\eta_I]\right]^m}{m!}\right], \tag{A.23}$$

and

$$\bar{\mathbb{I}}_3 = \sqrt{i} \int_{-[\eta_R+\eta_I]/\sqrt{2}}^{\infty} e^{-z_3^2} dz_3, \tag{A.24}$$

which can be rewritten as

$$\bar{\mathbb{I}}_3 = \frac{\sqrt{i\pi}}{2} \left[1 + Erf\left[[\eta_R + \eta_I]/\sqrt{2}\right]\right]. \tag{A.25}$$

This contour has the disadvantage of lengthening $\bar{\mathbb{I}}_1$. As a result, a few more terms in the summation must be kept.

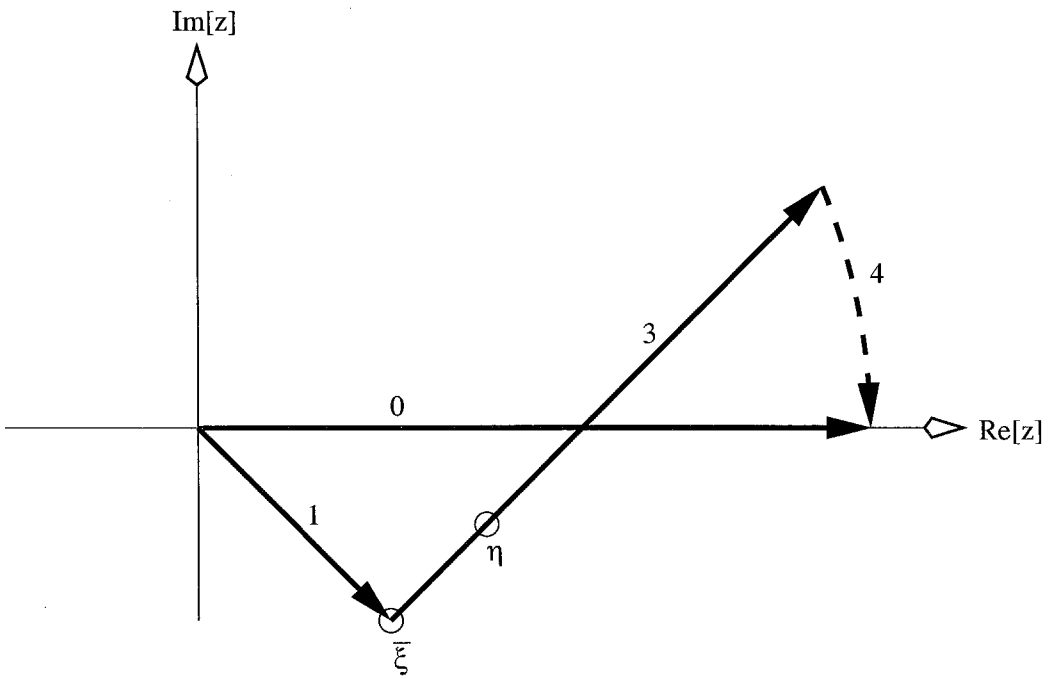

Figure A.2: Alternate contour. $\bar{\xi} \equiv \frac{[\eta_R - \eta_I]}{\sqrt{2i}}$

With an analytic expression for $E(t)$ in hand, standard non-linear fitting methods can be used to determine the parameters associated with observed resonance crossings. Data collected from the Hanford 2 km interferometer is shown in figure A.3 along with a fit using equation (A.25) and equation (A.23) including terms up to $n = 5$. The fit to this event indicates that the crossing velocity was 6.2 μm/ s, the demodulation phase 10° from optimal, and the cavity decay time is 835 μs (as opposed to the nominal value of 944 μs).

It is also worth noting that in all of these equations the scale is set by η. This fact can be used to define a critical velocity above which cavity dynamics become apparent. Choosing this point to be at $\eta_I = 1$ yields

$$v_{crit} = \frac{\gamma^2}{2Tk}. \tag{A.26}$$

The resonance crossing shown in figure A.3, for instance, has $v \sim 10 v_{crit}$. Crossings with $v < v_{crit}$ are well described by the adiabatic equations given in section A.1.

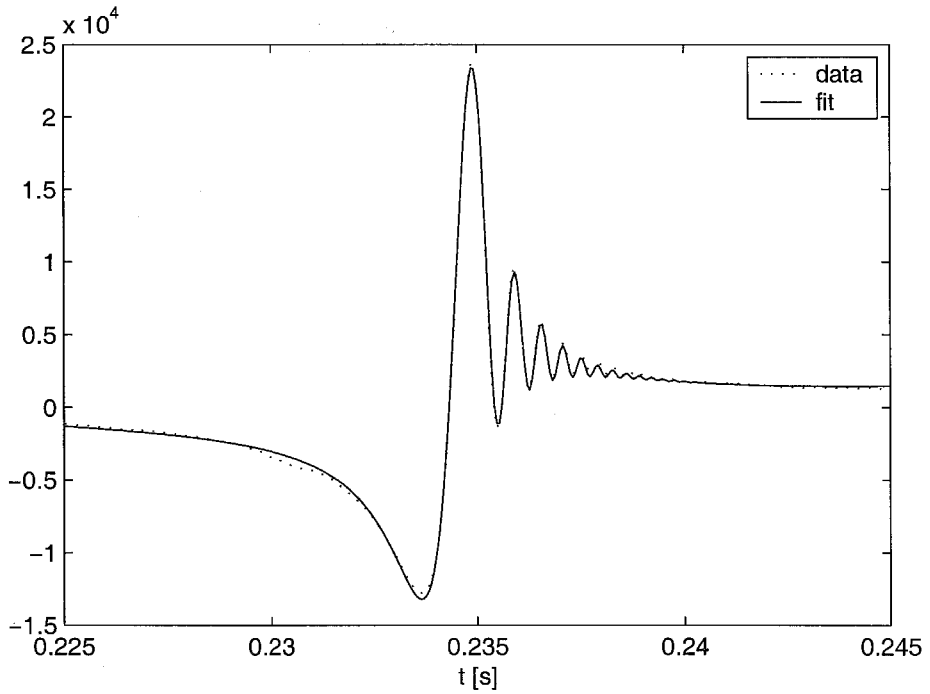

Figure A.3: Hanford 2 km cavity response to a fixed velocity sweep. The demod signal is fit using the alternate contour presented above, keeping the first seven terms in equation (A.23). Three additional fit parameters are used to describe a quadratic fit to a slowly varying offset in the measured signal due to the presence of other nearby resonances.

Appendix B

Notational Conventions

B.1 Notational Conventions

For the sake of clarity, if not readability, this work attempts to abide by a few simple notational conventions. Square brackets, [ ], are used in equations for grouping mathematical expressions. Parentheses, ( ), are reserved for specifying function arguments and curly brackets, { }, for delimiting sets. Matrices are delimited by double square brackets, $[\![\quad]\!]$. In some cases, the type of variable is indicated as follows: $\mathbf{S}$ matrix, $\vec{s}$ vector, $\bar{s}$ unitless ratio.

The use of complex variables is prevalent in this work. The lowercase letter i is used to represent the unit imaginary number. Function notation is used to express the real, $\mathcal{R}e()$, and imaginary, $\mathcal{I}m()$, parts of a complex variable or expression. Absolute value notation is used to express the magnitude of a complex variable or expression and * is used to indicate the complex conjugate as in the equation $|x|^2 = \mathcal{R}e(x)^2 + \mathcal{I}m(x)^2 = x\ x^\star$.

Unless otherwise specified, variables (e.g., positions and field amplitudes) are implicit functions of time. If an equation contains variables that are evaluated at different times, all evaluation times are specified explicitly.

B.2 Symbol Glossary

B.2.1 General

A_X	generic field amplitude on surface X
A_X^{bi}	incoming field amplitude on the back of surface X
A_X^{fi}	incoming field amplitude on the front of surface X
A_X^{bo}	outgoing field amplitude on the back of surface X
A_X^{fo}	outgoing field amplitude on the front of surface X
c	speed of light in vacuum
E_X	generic electric field on surface X
j	sideband index
k	wave number
P_X	generic field power on surface X
g	electronic gain or optical transduction gain
l, m, n, p, q	integer variables and numeric subscripts
$L_{X:Y}$	distance between reference planes of surfaces X and Y
r_X	amplitude reflectivity of surface X
t_X	amplitude transmissivity of surface X
z_X	position of surface X
α	optical mode overlap coefficient
λ	wavelength
ω	angular frequency

B.2.2 Chapter 1

h	gravitational wave strain
L	length over which strain is measured (e.g., interferometer arm length)
Δh	minimum measureable strain
ΔL	change in L due to h
$\Delta\phi$	noise in ϕ
ϕ	differential phase shift at the beam-splitter

B.2.3 Chapter 2

A_{IN}	field amplitude of field source
A_{IO_j}	field amplitudes of input field
A_{PD_j}	field amplitudes at a photodiode
$E_{IO}(t)$	electric field at interferometer input
$J_j(x)$	Bessel functions
S_{demod}	demod signal
Γ_{mod}	modulation depth
ϕ_{demod}	demodulation phase
ω_{IN}	angular frequency of field source
ω_{IO_j}	angular frequency of input field components (carrier and sidebands)
ω_{mod}	angular modulation frequency of input field

B.2.4 Chapter 3

IT	input test-mass
ET	end test-mass
$\mathcal{F}$	cavity finesse
REF	reflection photodiode
S_{Lin}	linearized error signal for a Fabry-Perot cavity
S_{PDH}	Pound-Drever-Hall reflection locking signal
TRN	transmission photodiode
v_{init}	initial velocity in lock acquisition simulations
Δ	length degree of freedom
Δ_{res}	value of Δ at carrier resonance points
ϕ_j	round-trip phase in a Fabry-Perot cavity

B.2.5 Chapter 4

ASY	antisymmetric photodiode
BS	beam-splitter
IT	input test-mass, transmitted side
IR	input test-mass, reflected side
ET	end test-mass, transmitted side
ER	end test-mass, reflected side
$\mathbf{G}$	input matrix
$\mathbf{M}$	sensing matrix
$\mathbf{M}_{FP}$	sensing matrix, Fabry-Perot cavity
$\mathbf{M}_{PR}$	sensing matrix, power-recycled
POB	beam-splitter pick-off photodiode
PR	power recycling mirror
REF	reflection photodiode
$\vec{S}_{demod}$	vector of demod signals
TRT	transmission photodiode, transmitted side
TRR	transmission photodiode, reflected side
$\vec{\Delta}$	vector of length degrees of freedom

B.3 Normalized Determinant

In order to use the determinant of a matrix not just as an indicator of arrival at a matrix singularity, but as a measure of the proximity of a singularity, it must be normalized. The normalized determinant given here is constructed such that scaling of any given row or column does not change its value.

For some set of indices $p_{m,n}$, the determinant of a matrix $\mathbf{M}$ can be expressed

$$|\mathbf{M}| = \sum_{n=1}^{N} (-1)^n \prod_{m=1}^{N} \mathbf{M}_{m,p_{m,n}}. \tag{B.1}$$

For the same $p_{m,n}$, the normalized determinant is

$$\widehat{|\mathbf{M}|} = \frac{\sum_{n=1}^{N}(-1)^n \prod_{m=1}^{N} \mathbf{M}_{m,p_{m,n}}}{\sum_{n=1}^{N} \left|\prod_{m=1}^{N} \mathbf{M}_{m,p_{m,n}}\right|} \tag{B.2}$$

such that

$$-1 \leq \widehat{|\mathbf{M}|} \leq 1. \tag{B.3}$$

Bibliography

[1] Luca Matone. *Étude du Contrôle Global de l'Interféromètre Central de VIRGO.* PhD thesis, L'Université Paris Xi Orsay, 1999.

[2] Nergis Mavalvala. *Alignment Issues in Laser-Interferometric Gravitational Wave Detectors.* PhD thesis, Massachusetts Institute of Technology, 1997.

[3] M. Evans, S.B. Anderson, K. Blackburn, A. Lazzarini, and T.A. Prince. Empirical estimates of ns-ns merger rates in the galaxy. In J. Tran Thanh Van, J. Dumarchez, S. Reynaud, C. Salomon, S. Thorsett, and J.Y. Vinet, editors, *Gravitational Waves and Experimental Gravity: Proceedings of the XXXIVth Recontres de Moriond*, pages 349–354, 2000.

[4] M.E. Gertsenshtein and V.I. Pustovoit. On the detection of low-frequency gravitational waves. *Soviet Physics - JETP*, 16:433, 1963.

[5] Kip S. Thorne. *Black Holes and Time Warps: Einstein's Outrageous Legacy.* W.W. Norton & Co., 1994.

[6] G.E. Moss, L.R. Miller, and R.L. Forward. Photon-noise-limited laser transducer for gravitational antenna. *Appl. Opt.*, 10:2495–2498, 1971.

[7] R. Weiss. Electromagnetically coupled broadband gravitational antenna. Research Laboratory of Electronics, Massachusetts Institute of Technology, Quarterly Progress Report No. 105, 1972.

[8] R.W.P. Drever. Interferometric detectors for gravitational radiation. In N. Deruelle and T. Piran, editors, *Gravitational Radiation*, pages 321–338. North Holland, Amsterdam, 1983.

[9] B.J. Meers. Recycling in laser-interferometric gravitational-wave detectors. *Phys. Rev. D*, 38(8):2317–2326, 1988.

[10] L. Schnupp. A talk delivered at *European Collaboration Meeting on Interferometric Detection of Gravitational Waves.* Sorrento, 1988.

[11] T.T. Lyons, M.W. Regehr, and F.J. Raab. Quantum limited optical phase detection at the 10^{-10} radian level. *JOSA A*, 2001.

[12] Peter R. Saulson. *Fundamentals of Interferometric Gravitational Wave Detectors.* World Scientific, 1994.

[13] Masaki Ando and Kimio Tsubono. TAMA Project: Design and Current Status. In Syd Meshkov, editor, *Gravitational Waves*, Third Edoardo Amaldi Conference, pages 128–139, 1999.

[14] R.W.P. Drever, G.M. Ford, J. Hough, I.M. Kerr, A.J. Munley, J.R. Pugh, N.A. Robertson, and H. Ward. A gravity-wave detector using optical cavity sensing. 9th International Conference on General Relativity and Gravitation at Jena, GDR, 1980.

[15] Jordan Camp, Lisa Seivers, Rolf Bork, and Jay Heefner. Guided lock acquisition in a suspended fabry-perot cavity. *Optics Letters*, 20(24):2463–2465, 1995.

[16] Brian J. Meers and Kenneth A. Strain. Modulation, signal, and quantum noise in interferometers. *Phys. Rev. A*, 44(7):4693–4703, 1991.

[17] T.T. Lyons, M.W. Regehr, and F.J. Raab. Shot noise in gravitational-wave detectors with Fabry-Perot arms. *Optics Letters*, 2000.

[18] James Mason. *Signal Extraction and Optical Design for an Advanced Gravitational Wave Interferometer.* PhD thesis, California Institute of Technology, 2001.

[19] M.W. Coles. The status of ligo. In Syd Meshkov, editor, *Gravitational Waves*, Third Edoardo Amaldi Conference, pages 101–109, 1999.

[20] Frédérique Marion for the VIRGO collaboration. Status of the VIRGO Experiment. In Syd Meshkov, editor, *Gravitational Waves*, Third Edoardo Amaldi Conference, pages 110–119, 1999.

[21] Martin Regehr. *Signal Extraction and Control for an Interferometric Gravitational Wave Detector.* PhD thesis, California Institute of Technology, 1995.

[22] Torrey T. Lyons. *An Optically Recombined Laser Interferometer for Gravitational Wave Detection.* PhD thesis, California Institute of Technology, 1997.

[23] Gehard Heinzel. *Advanced optical techniques for laser interferometric gravitational wave detectors.* PhD thesis, University of Hannover, 1999.

[24] A. E. Siegman. *Lasers.* University Science, California, 1986.

[25] H. Yamamoto and et al. End to end simulation program for gravitational-wave detectors. In Seiji Kawamura and Norikatsu Mio, editors, *Gravitational Wave Detection II*, Frontiers Science Series No. 32, pages 331–336, 2000.

[26] P. Fritschel, M. Zucker, R. Bork, N. Mavalvala, D. Ouimette, G. Gonzalez, H. Rong, and D. Sigg. Readout and control of a power-recycled interferometric gravitational wave antenna. *JOSA A*, page submitted, 2001.

[27] A. Rüdiger, R. Schilling, L. Schnupp, W. Winkler, H. Billing, and K. Maischberger. A mode selector to suppress fluctuations in laser beam geometry. *Optica Acta*, 28(5):641–658, 1981.

[28] Malik Rakhmanov. Doppler-induced dynamics of fields in fabry perot cavities with suspended mirrors. *Applied Optics*, 40(12):1942, 2001.